12-2019

Quantitative Analysis Techniques for Assessing Organelle Organization and Dynamics in Individual Cells

Isaac Vargas
University of Arkansas, Fayetteville

Quantitative Analysis Techniques for Assessing Organelle Organization and Dynamics in Individual Cells

A thesis submitted in partial fulfillment
of the requirements for the degree of
Master of Science in Biomedical Engineering

by

Isaac Vargas
University of Arkansas
Bachelor of Science in Biomedical Engineering, 2017

December 2019
University of Arkansas

This thesis is approved for recommendation to the Graduate Council.

_____
Kyle P. Quinn, Ph.D.
Thesis Director

_____
Narasimhan Rajaram, Ph.D.
Committee Member

_____
Kartik Balachandran, Ph.D.
Committee Member

_____
Shilpa Iyer, Ph.D.
Committee Member

ABSTRACT

In biomedical optics and microscopy, the organization and morphology of organelles have been widely studied. In spite of novel imaging techniques, there is still a lack of quantitative tools to easily measure cellular characteristics from image data. Previous studies have explored multiple approaches to assess organelle organization and alignment, resulting in complicated and extensive algorithms that are both subject to multiple steps of image processing and influenced by non-cellular artifacts. In this thesis, a technique called the Modified Blanket Method (MBM) is introduced to quantify organelle organization through measurements of fractal dimension (FD) on a pixel-by-pixel basis. With the use of simulated fractal clouds, it is demonstrated that the MBM is capable of accurately and rapidly quantify FD, having a higher sensitivity to a wider range of FD values compared to previous methods. Furthermore, the MBM could differentiate mitochondrial organization of radiation-resistant A549 lung cancer cells at different time points post-radiation.

In later experiments, the MBM is combined with similar computational techniques to quantify fiber alignment and nuclear shape through measurements of directional variance (DV) and nuclear aspect ratio (NAR). The simultaneous use of these tools demonstrated that the organization and alignment of mitochondria and actin of NIH 3T3 cells treated with L-buthionine-sulfoximine (BSO) change over time, having different nuclear shapes as well. It is then concluded the this set of computational tools is capable of providing significant cellular data, which could potentially be employed to understand the cellular dynamics of multiple pathological conditions such as diabetes, Alzheimer's, Leigh's syndrome, and myopathy, all of which are known to be influenced by dysfunctional organelles.

ACKNOWLEDGEMENTS

I would like to thank every single member of the Quinn lab for their help and support through this program. I will always be thankful for the mentorship and patience provided by Dr. Kyle Quinn during both my undergraduate and graduate programs. I would especially like to thank my lab mentors Olivia Kolenc, Jake Jones, Hallie Toomer, and Alan Woessner for always being helpful and leading me through my studies and experiments.

DEDICATION

To my beloved parents, Luis Vargas and Rosemary Lopez de Vargas, for their constant and unconditional support. To my exemplary brothers, Luis Vargas and Ivan Vargas, whose advice was always prudent and encouraging. And to my friends in both the United States and Panama whose help and love were at all times inspiring throughout the years.

TABLE OF CONTENTS

LIST OF FIGURES

LIST OF TABLES

LIST OF PUBLISHED PAPERS

CHAPTER 2

1. Vargas, I., et al., Rapid quantification of mitochondrial fractal dimension in individual cells. Biomed Opt Express, 2018. 9(11): p. 5269-5279.

CHAPTER 1

INTRODUCTION

1.1 Motivation for this Research

The organization and morphology of organelles have been of major interest in biomedical sciences in recent years [1-3]. Understanding the dynamics of cellular components have significantly contributed to the diagnoses and development of treatments of multiple pathological disorders [4-6]. Biologically, assessments with techniques such Seahorse [7, 8], ELISA [9, 10], and gel electrophoresis [11] have made it possible to interpret the physiological and molecular properties of many of these conditions. In addition, thanks to the latest advancements of technology and the inclusion of sophisticated imaging techniques through the use of optics and microscopy, it is now possible to correlate what is known from biology with the visible behavior of specific cellular structures and organelles as they interact to both internal and external stimuli [12, 13]. For example, multiple studies have employed fluorescent microscopy to isolate organelles such as the mitochondria as they evaluate the properties and changes experienced under certain conditions [14-16]. Similarly, structural components such as the cytoskeleton have been studied to understand its role in maintaining a proper cell membrane [17, 18]. Also, a vast number of studies employ imaging techniques just to visually differentiate cells [19, 20].

Multiphoton and laser scanning confocal microscopes are able to acquire state of the art images that clearly depict some of the intrinsic characteristics of multiple cellular structures [21, 22]. Because of this, a wide variety of published studies have employed image processing techniques such as skeletonization [23], power spectral density [24], and fiber orientation [25, 26] to assess organelle properties from this type of images through computational algorithms. However, most of the current image analysis techniques are still difficult to apply and require

multiple steps of pre-processing prior to the actual quantification. As a result, there is still a lack of quantitative tools capable of easily, rapidly, and simultaneously measuring organelle characteristics. Because of this, the motivation behind this research was to explore and develop new techniques to potentially overcome these obstacles and assess organelle dynamics in a rapid and accurate manner.

1.2 Objective of Thesis

The objective of this thesis is to introduce new automated computational tools that are able to rapidly quantify multiple organelle characteristics in conjunction. Following this, programming using MATLAB was utilized to develop and execute three different types of cellular assessments: organization through fractal dimension (FD) [27], fiber orientation and alignment through directional variance (DV) [28, 29], and nuclear shape through nuclear aspect ratio (NAR) [30].

1.3 Organization of Thesis

The first part of this thesis focuses on the Modified Blanket Method (MBM), which is initially introduced to measure mitochondrial fractal dimension (FD) of both simulated and A549 lung cancer cells while being compared to a previously published technique called power spectral density (PSD) [24, 27]. The second part of the thesis explores the organization and alignment of mitochondria and actin, as well as the nuclear shape of of NIH 3T3 cells. Using L-buthionine-sulfoximine (BSO), cellular changes were induced for a period of 24 hours. FD, DV, NAR measurements were simultaneously obtained using the developed set of tools and then correlated to understand the relationship between actin, mitochondria, and cell nuclei as the cells are exposed to different treatment concentrations.

1.4 References

1. Itzkan, I., et al., Confocal light absorption and scattering spectroscopic microscopy monitors organelles in live cells with no exogenous labels. Proc Natl Acad Sci U S A, 2007. **104**(44): p. 17255-60.

2. Pyhtila, J.W., R.N. Graf, and A. Wax, Determining nuclear morphology using an improved angle-resolved low coherence interferometry system. Optics Express, 2003. **11**(25): p. 3473-3484.

3. Ding, H., et al., Actin-driven cell dynamics probed by Fourier transform light scattering. Biomed Opt Express, 2010. **1**(1): p. 260-267.

4. Clarkson, E., C.F. Costa, and L.M. Machesky, Congenital myopathies: diseases of the actin cytoskeleton. J Pathol, 2004. **204**(4): p. 407-17.

5. Muraresku, C.C., E.M. McCormick, and M.J. Falk, Mitochondrial Disease: Advances in clinical diagnosis, management, therapeutic development, and preventative strategies. Curr Genet Med Rep, 2018. **6**(2): p. 62-72.

6. McFarland, R. and D.M. Turnbull, Batteries not included: diagnosis and management of mitochondrial disease. J Intern Med, 2009. **265**(2): p. 210-28.

7. Iuso, A., et al., Assessing Mitochondrial Bioenergetics in Isolated Mitochondria from Various Mouse Tissues Using Seahorse XF96 Analyzer. Methods Mol Biol, 2017. **1567**: p. 217-230.

8. Divakaruni, A.S., G.W. Rogers, and A.N. Murphy, Measuring Mitochondrial Function in Permeabilized Cells Using the Seahorse XF Analyzer or a Clark-Type Oxygen Electrode. Curr Protoc Toxicol, 2014. **60**: p. 25 2 1-16.

9. Frankfurt, O.S. and A. Krishan, Enzyme-linked immunosorbent assay (ELISA) for the specific detection of apoptotic cells and its application to rapid drug screening. J Immunol Methods, 2001. **253**(1-2): p. 133-44.

10. Rahimi, M.T., et al., Evaluation of Fast-ELISA versus standard-ELISA to diagnose human fasciolosis. Arch Iran Med, 2011. **14**(1): p. 18-21.

11. Korkko, J., et al., Sensitivity of conformation sensitive gel electrophoresis in detecting mutations in Marfan syndrome and related conditions. J Med Genet, 2002. **39**(1): p. 34-41.

12. Sorensen, C.E. and I. Novak, Visualization of ATP release in pancreatic acini in response to cholinergic stimulus. Use of fluorescent probes and confocal microscopy. J Biol Chem, 2001. **276**(35): p. 32925-32.

13. Lahn, M., C. Dosche, and C. Hille, Two-photon microscopy and fluorescence lifetime imaging reveal stimulus-induced intracellular Na+ and Cl- changes in cockroach salivary acinar cells. Am J Physiol Cell Physiol, 2011. **300**(6): p. C1323-36.

14. Clutton, G., et al., A Reproducible, Objective Method Using MitoTracker(R) Fluorescent Dyes to Assess Mitochondrial Mass in T Cells by Flow Cytometry. Cytometry A, 2019. **95**(4): p. 450-456.

15. Pendergrass, W., N. Wolf, and M. Poot, Efficacy of MitoTracker Green and CMXrosamine to measure changes in mitochondrial membrane potentials in living cells and tissues. Cytometry A, 2004. **61**(2): p. 162-9.

16. Buckman, J.F., et al., MitoTracker labeling in primary neuronal and astrocytic cultures: influence of mitochondrial membrane potential and oxidants. J Neurosci Methods, 2001. **104**(2): p. 165-76.

17. Saarikangas, J., H. Zhao, and P. Lappalainen, Regulation of the actin cytoskeleton-plasma membrane interplay by phosphoinositides. Physiol Rev, 2010. **90**(1): p. 259-89.

18. Boulant, S., et al., Actin dynamics counteract membrane tension during clathrin-mediated endocytosis. Nat Cell Biol, 2011. **13**(9): p. 1124-31.

19. Konig, K., A. Uchugonova, and E. Gorjup, Multiphoton fluorescence lifetime imaging of 3D-stem cell spheroids during differentiation. Microsc Res Tech, 2011. **74**(1): p. 9-17.

20. Rice, W.L., D.L. Kaplan, and I. Georgakoudi, Quantitative biomarkers of stem cell differentiation based on intrinsic two-photon excited fluorescence. J Biomed Opt, 2007. **12**(6): p. 060504.

21. Kolenc, O.I. and K.P. Quinn, Evaluating Cell Metabolism Through Autofluorescence Imaging of NAD(P)H and FAD. Antioxid Redox Signal, 2019. **30**(6): p. 875-889.

22. Yi, Q. and M.G. Coppolino, Automated classification and quantification of F-actin-containing ruffles in confocal micrographs. Biotechniques, 2006. **40**(6): p. 745-6, 748, 750 passim.

23. Valente, A.J., et al., A simple ImageJ macro tool for analyzing mitochondrial network morphology in mammalian cell culture. Acta Histochem, 2017. **119**(3): p. 315-326.

24. Xylas, J., et al., Improved Fourier-based characterization of intracellular fractal features. Opt Express, 2012. **20**(21): p. 23442-55.

25. Birkholz, H., et al. Quantification of Actin Filament Organization by Estimating Graph Structures in Confocal Microscopic Images. in World Congress on Medical Physics and Biomedical Engineering, September 7 - 12, 2009, Munich, Germany. 2010. Berlin, Heidelberg: Springer Berlin Heidelberg.

26. Marquez, J.P., Fourier analysis and automated measurement of cell and fiber angular orientation distributions. International Journal of Solids and Structures, 2006. **43**(21): p. 6413-6423.

27. Vargas, I., et al., Rapid quantification of mitochondrial fractal dimension in individual cells. Biomed Opt Express, 2018. **9**(11): p. 5269-5279.

28. Quinn, K.P., et al., An automated image processing method to quantify collagen fibre organization within cutaneous scar tissue. Exp Dermatol, 2015. **24**(1): p. 78-80.

29. Quinn, K.P. and I. Georgakoudi, Rapid quantification of pixel-wise fiber orientation data in micrographs. J Biomed Opt, 2013. **18**(4): p. 046003.

30. Lam, N.T., et al., Valve interstitial cell contractile strength and metabolic state are dependent on its shape. Integr Biol (Camb), 2016. **8**(10): p. 1079-1089.

CHAPTER 2

RAPID QUANTIFICATION OF MITOCHONDRIAL FRACTAL DIMENSION IN INDIVIDUAL CELLS

Vargas, I., et al., Rapid quantification of mitochondrial fractal dimension in individual cells. Biomed Opt Express, 2018. **9**(11): p. 5269-5279.

Submitted as an original article by:

Isaac Vargas,[1] Kinan Alhallak,[1] Olivia I. Kolenc,[1] Samir V. Jenkins,[2] Robert J. Griffin,[2] Ruud P. M. Dings,[2] Narasimhan Rajaram,[1] and Kyle P. Quinn[1,*]

[1]Department of Biomedical Engineering, University of Arkansas, Fayetteville, AR 72701, USA

[2]Division of Radiation Biology, University of Arkansas for Medical Sciences, Little Rock, AR 72205, USA

Corresponding author:

Kyle P. Quinn, PhD

Department of Biomedical Engineering

University of Arkansas

123 John A. White Jr. Engineering Hall

Fayetteville AR 72701

Tel: +1 479 575 5364

Fax: +1 479 575 4346

*E-mail: kpquinn@uark.edu

Abstract

An improved technique for fractal characterization called the Modified Blanket method is introduced which can quantify surrounding fractal structures on a pixel by pixel basis without artifacts associated with scale-dependent image features such as object size. The method interprets images as topographical maps, obtaining information regarding the local surface area as a function of image resolution. Local fractal dimension (FD) can be quantified from the power law exponent derived from the surface area and image resolution relationship. We apply this technique on simulated cell images of known FD and compared the obtained values to power spectral density (PSD) analysis. Our method is sensitive to a wider FD range (2.0 – 4.5) having a mean error of 1.4% compared to 6% for PSD analysis. This increased sensitivity and an ability to compute regional FD properties enabled the discrimination of differences in radiation resistant cancer cell responses that could not be detected using PSD analysis.

2.1 Introduction

Fractal patterns are very common in nature and can be observed in different types of biological structures and functions [1, 2]. Image analysis of these self-repeating patterns over length- or time-scales is an attractive approach to quantify changes in biological structures [3]. For example, mitochondria undergo fission and fusion based on the metabolic needs of the cell [4], and it has been demonstrated that mitochondrial organization follows the statistical properties of self-similar fractals [5-8]. Previous studies have demonstrated that mitochondrial reorganization occurs in a wide variety of pathological conditions, including Parkinson's disease [5, 9], cancer [4, 6, 10-15], and mitochondrial diseases [16]. However, there are several challenges in quantifying the fractal organization of organelles within cells.

Various techniques have been developed to estimate fractal dimension. One of the oldest and simplest approaches for fractal analysis is known as the box counting method, which superimposes boxes of decreasing size over a region of interest within an image [17]. The power law relationship between the number of boxes intersected by the pattern of interest and the size of the boxes is used to estimate fractal organization [1, 17]. However, box counting can only be performed on binary images and is most commonly used to characterize the border of objects. To quantify the fractal dimension of grayscale images, Fourier-based approaches have been used, particularly in mitochondrial clustering analysis. Through radial sampling of two-dimensional power spectral density (PSD) maps, fractal dimension (FD) can be determined from images by measuring the exponent, β, from the power law relationship between PSD and spatial frequency as shown in Eq. (1) [8].

$$R\left(\vec{k}\right) = A\left(\vec{k}\right)^{-\beta} \tag{1}$$

This PSD approach can be used to quantify mitochondrial textures within cells through a pre-processing step that segments cells and replicates intracellular patterns in the background of images, providing accurate measurements of mitochondrial organization over a range of FD or β values. Using this approach, Xylas et al. [10] calculated the power exponent β from NADH autofluorescence images as a measure of mitochondrial clustering and identified depth-dependent changes between normal and precancerous epithelial tissue. Pouli et al. [4] also utilized PSD analysis to evaluate mitochondrial dynamics from NADH intensity images in different epidermal layers of human skin. Similarly, Liu et al. [18] used PSD analysis of NADH images to measure mitochondrial clustering in relation to structural metabolic changes caused by controlled perturbations such as extrinsic and intrinsic mitochondrial uncoupling, glycolysis, and fatty acid oxidation. However, this PSD approach is susceptible to errors when cell segmentation

is inaccurate and scale-dependent features remain visible after pre-processing. Furthermore, the PSD approach is also only able to obtain the overall FD of an image and cannot provide region-specific information, such as the FD of individual cells. To overcome these issues, MacDonald et al. [7], utilized an autocorrelation technique capable of analyzing patterns within individual cells. However, this autocorrelation technique is particularly time consuming and not suitable for mapping FD in large image sets.

The goal of our study was to develop a rapid and automated method for quantifying fractal patterns within images on a pixel-by-pixel basis. We modified a previously developed technique known as the Blanket method [11, 19, 20]. The Blanket method interprets images as a three-dimensional surface topography, where the intensity at each pixel corresponds to the height along the z axis. The surface area (SA) of the topographic map is computed as a function of scale (pixel size) [11, 21], and the power law relationship between SA and pixel size is used to determine FD. Caldwell et al. [11] and Byng et al. [19] employed this approach for the fractal analysis of mammographic parenchymal morphologies, which are strongly related to the development of breast cancer. Chappard et al. [22] also used the Blanket method to characterize the texture of trabecular bone in X-Rays. In the current study, we propose a Modified Blanket Method (MBM), which utilizes convolution to rapidly compute local measurements of SA, and thus produce maps of FD within images. By acquiring local FD values at each pixel, the analysis of specific structures or individual cells is possible. Here, we present a series of studies in which we analyze simulated cell images containing fractal patterns of known FD to show that the MBM is sensitive to a wide range of FD values. We evaluate the effects of different convolution kernels on the accuracy of the FD measurements and compare them to PSD analysis. Moreover,

we demonstrate the biomedical application of the MBM on NADH autofluorescence images obtained from parental and radiation resistant A549 lung cancer cells.

2.2 Methods

2.2.1 Modified Blanket Method

The MBM was developed as an automated technique to convolve gradient images at different resolutions and compute FD. The image analysis algorithm was coded and executed in MATLAB. The length scale over which the local fractal dimension is analyzed is based on a convolution kernel defined by a binary disk with a user-defined radius. The algorithm begins by resampling both the image of interest and convolution kernel (Fig. 2.1a) proportionally. The number times the image is resampled at different image resolutions is determined by the size of the kernel. Once the image has been resampled, the horizontal (X) and vertical (Y) gradients of the image are computed using X- and Y- gradient kernels [1,-1,0] and $[0,-1,1]^T$ respectively (Fig. 2.1b). The absolute value of the gradient in the X- and Y- directions are then summed by convolving with a binary disk kernel (Fig. 2.1c). The summed horizontal and vertical gradients are added together to compute a local surface area (SA) map (Fig. 2.1d). This SA map is subsequently resampled back to the original dimensions of the image and stored (Fig. 2.1e). These steps (Fig. 2.1a-e) are repeated as the convolution kernel is reduced in size by increments of 1 pixel until a 1x1 kernel remains, ultimately producing a set of SA maps derived from different image resolutions (Fig. 2.1f). The power law exponent (β) relating local surface area measurements and pixel sizes at each pixel location can be derived from the linear change in log-transformed values between SA maps (Fig. 2.1g). Fractal dimension at each pixel location (Fig. 2.1g) can then be determined through the equation:

$$FD = 2 - \frac{\Delta \log (SA)}{\Delta \log (\textit{pixel size})} = 2 - \beta \tag{2}$$

In order to observe the changes in local fractal dimension, a FD map (Fig. 2.1h) can be generated by assigning the corresponding FD value to each individual pixel.

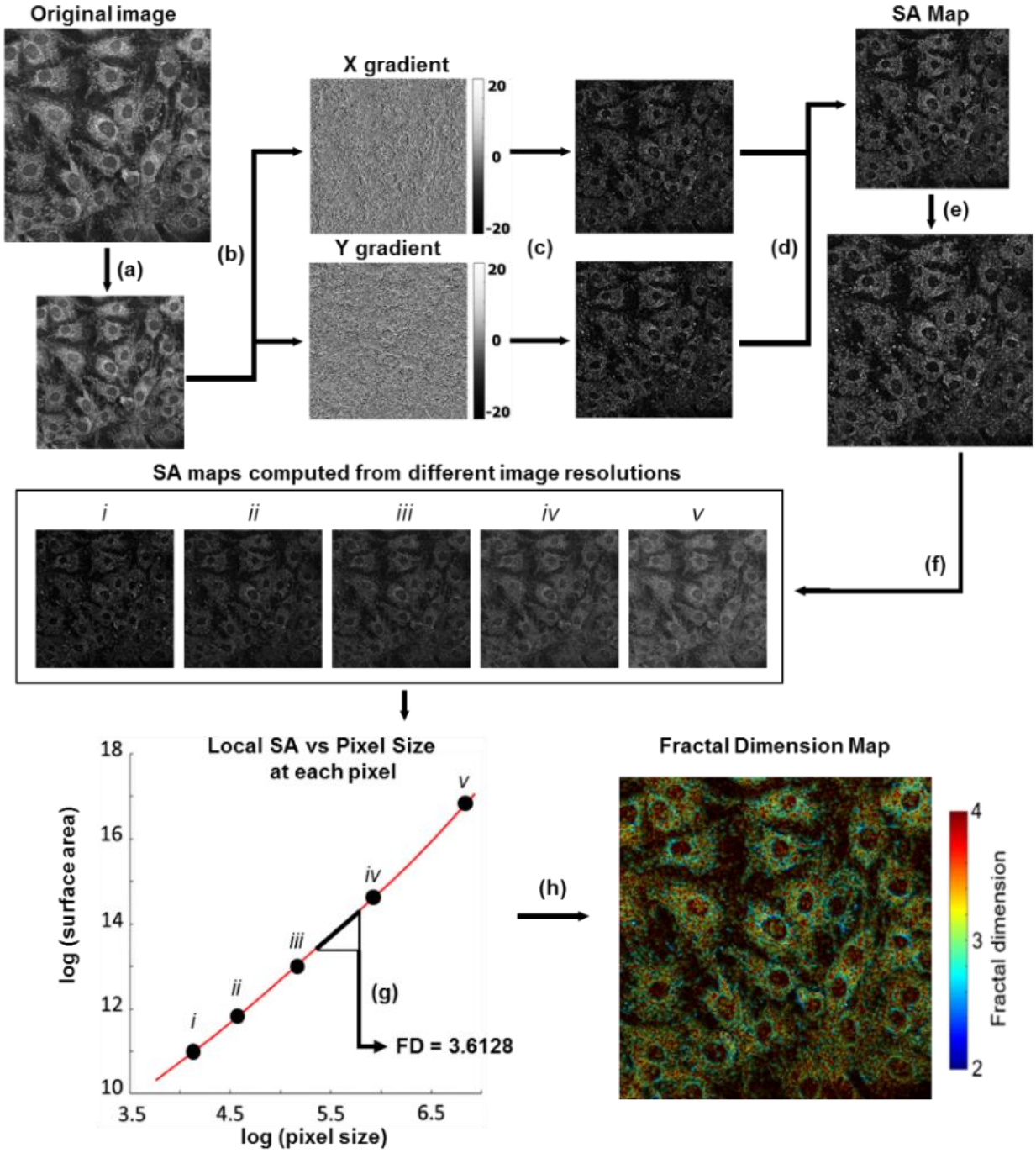

Figure 2.1. Steps of the Modified Blanket Method. **(a)** Resize the image of interest and a disk kernel. **(b)** Compute the horizontal (x) and vertical (y) gradients of the image. **(c)** Convolve the absolute value of each gradient image with a disk kernel to sum up local changes in intensity. **(d)** Compute the sum of the convolved x- and y- gradient images to create a surface area (SA) map. **(e)** Resize the SA map to the original image size, and record SA at each pixel. **(f)** Repeat steps (a)-(e) at different image resolutions (i.e. pixel sizes) to produce a set of SA maps. **(g)** Compute the FD from the power law exponent of the local surface area vs. pixel size curve at each pixel. **(h)** Assign the corresponding FD value to each pixel to produce a FD map.

2.2.2 Validation: Simulated cell images

To assess the accuracy of the MBM to approximate fractal values, we created simulated cells containing intensity clouds of known fractal dimension as in previous studies [8]. The fractal clouds were obtained by filtering white noise in the frequency domain and transforming it back to the spatial domain [8]. These fractal clouds were overlaid using masks of circular cells with varying diameter and cellular nuclei. We evaluated these simulated cell images over a range of fractal dimension values (FD=2.0 to FD=4.5) and cell diameters (d=80, d=120, and d=160 pixels) commonly observed in biomedical images. FD values were obtained from five repetitions of each combination of FD and cell diameter. The fractal clouds and cell positions were randomized during each repetition of the simulation, and FD was derived using our MBM method. This process was then repeated for three different cell densities (10, 20, and 30% of the total image area) to measure differences caused by increasing cell quantities. Mean error and standard deviation were computed using the measured FD values obtained from the simulation repetitions.

In addition to the varying fractal clouds and cell diameters, we analyzed the simulated cell images over a range of different convolution radii (CR=5, CR=10, CR=15, and CR=20 pixels) to obtain local fractal dimension values. Errors in FD measurements associated with abrupt intensity changes at cell borders have been previously described [8] and at larger CR values it is possible to visualize these edge effects. In order to estimate the differences in the average FD caused by such artifacts, we examined the effect of cell mask erosion to isolate the regions of interest (i.e. the center of simulated cells) from edge effects. We ran simulations with different combinations of convolution radii (CR) and erosion radii (ER) and computed the average FD (Fig. 2.2).

2.2.3 Comparison to Power Spectral Density approach

To compare the results obtained with the MBM, we also employed PSD analysis as in previous work [4, 8, 10, 18]. The PSD approach computes a radial average of the 2D Fourier transform of the image, resulting in a 1D PSD curve [8]. To reduce abnormalities caused by regions that do not contain intercellular features, a clone stamping pre-processing step was used, which fills the background with copies of the intracellular image features [8]. The 1D PSD curve was fit to a specific range of frequency values, corresponding to the most linear portion of the plot as in previous studies [4, 8]. The power law exponent (β) commonly reported in other studies [1, 8] can be related to fractal dimension using Eq. (3).

$$FD = \frac{(8 - \beta)}{2} \tag{3}$$

The accuracy of both methods (MBM and PSD) over a wide range of FD values (FD=2.0 to FD=4.5) was evaluated using the simulated cell images. The computational time of each method was also measured using five repetitions at different image resolutions (128 x 128, 256 x 256, 512 x 512, 1024 x 1024, 2048 x 2048, and 4096 x 4096 pixels). For the MBM, we evaluated three different CR values (CR=5, CR=10, and CR=25) to assess their effect on the speed of the fractal analysis. The computational times recorded at each repetition were then used to compute mean times and their standard deviation.

2.2.4 Biomedical application to understanding cancer metabolism

To demonstrate the sensitivity of this MBM technique using experimental data, we compared FD values obtained from NADH autofluorescence images of cell mitochondria from parental and radiation-resistant A549 lung cancer cells. In order to generate radiation resistant A549 cells, the parental cell line was subjected to multiple doses of 2 Gy radiation [23]. Images

from both cell lines were then acquired at different post-radiation time points (t=0, t=1, t=12, and t=24 hours), with a total of nine images per time period. Two-photon excited fluorescence from NADH was collected using a 20x water-immersion objective (NA=0.75) with a 460/40 nm bandpass filter and a Ti:Sapphire laser source tuned to 755 nm. Image resolution was set to 512 x 512 pixels (130 μm x 130 μm) with 16-bit depth. FD values were obtained using both the MBM and PSD method.

2.2.5 Statistical Analysis

An ANOVA design with image fields nested within cell culture dishes was used to identify differences in FD between cell lines (parental and radiation-resistant) and time points. Significance was based on an α=0.05.

2.3 Results

2.3.1 Method Validation

Utilizing simulated microscopy images of cells with intracellular fractal clouds of known FD, we demonstrated that the MBM can compute FD values that successfully estimate true FDs ranging from 2.00 to 4.50 (Fig. 2.2a, b). For 120 pixel diameter simulated cells, a CR of 5 produced a mean error of 1.4±1.0%. However, increasing the convolution radius (CR) over which the FD is computed slightly decreased accuracy (Fig. 2.2a), with mean errors of 2.1±1.9%, 3.6±3.3% and 5.0±3.7% for radii of 10, 15 and 20, respectively. The FD values obtained from the MBM were insensitive to differences in cell size (d=80, d=120, and d=160 pixels), cell density (10, 20, and 30% cell coverage per image), or overall image intensity. Using cell images with FD=2.5, the MBM analysis resulted in a mean error of 0.72±0.49%, 1.08±0.34%, and 1.76±0.76% for cell diameters of 80, 120, and 160 pixels respectively. A similar analysis was

performed with varied cell densities, resulting in a mean error of 1.97±0.88%, 2.07±0.78%, and 2.14±0.54% for 10, 20, and 30% cell coverage respectively.

Mean error in average FD measurements from simulated cell images also significantly increased if the cell borders were not removed from analysis through the morphological operation of erosion (Fig. 2.2c). When using a CR of 5, the lack of an erosion step prior to FD averaging resulted in a mean error of 3.6±2.6%. This error was even greater for CR of 10, which increased error from 2.1±1.9% to 7.1±4.5% (Fig. 2.2d). Pixelwise FD maps indicate that inaccurate measurements of FD approaching a value of 2 are observed along the cell-background border (Fig. 2.2e) in simulated images. An erosion radius equivalent to the convolution radius is necessary to remove these artifacts produced when abrupt, non-fractal changes in image intensity are present.

Unlike the MBM, PSD analysis was not accurate at FDs below 2.75 (Fig. 2.3a). While the MBM had a mean error of 1.4±1.0% and maximum error of 4.26% over FDs from 2.0-4.5, PSD yielded a mean error of 6.0±10.9% and maximum error of 35.50% (Fig. 2.3a, b). The MBM was also able to compute FD with significantly shorter computational times than the PSD approach, particularly at image resolutions of 1024x1024 and higher (Fig. 2.3). MBM analysis with CR=5 had computational times on a standard desktop computer that were up to 42-times faster on 4096x4096 images and 3-times faster on 128x128 images than PSD analysis. Increasing the CR resulted in longer computational times, but CR=10 was still 17-times faster than PSD analysis of 4096x4096 images and 1.5-times faster on 128x128 images (Fig. 2.4). For both the PSD and MBM, image resolution and computational time scaled according to a power law.

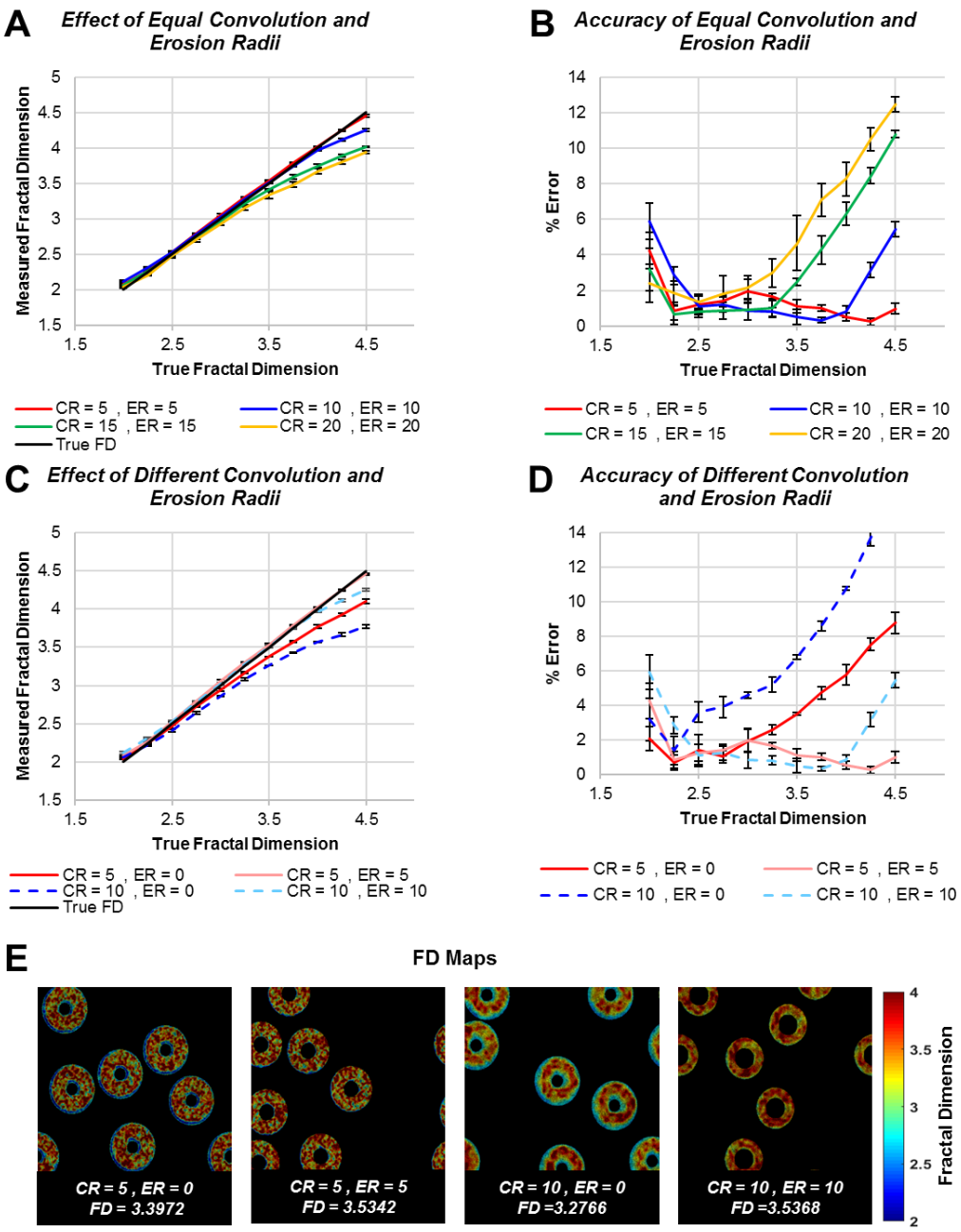

Figure 2.2. Modified Blanket Method Simulation. **(A)** Effect of utilizing convolution and erosion radii (CR & ER) of equal size in the measured fractal dimension of cells with a diameter of 120 pixels. The black line represents the true FD. **(B)** Effect of utilizing convolution and erosion radii of varied size in the measured fractal dimension. Red lines represent CR=5, Blue lines represent CR=10. Erosion radius is set to ER=0, 5, or 10. (**C)** Percentage error of the analysis with equal convolution and erosion radii size. **(D)** Percentage error of the analysis with varied convolution and erosion radii size. **(E)** Representative FD maps with a true FD value of 3.5 show the edge effects produced by cell boundaries when cell mask erosion is not applied prior to computing the average FD value.

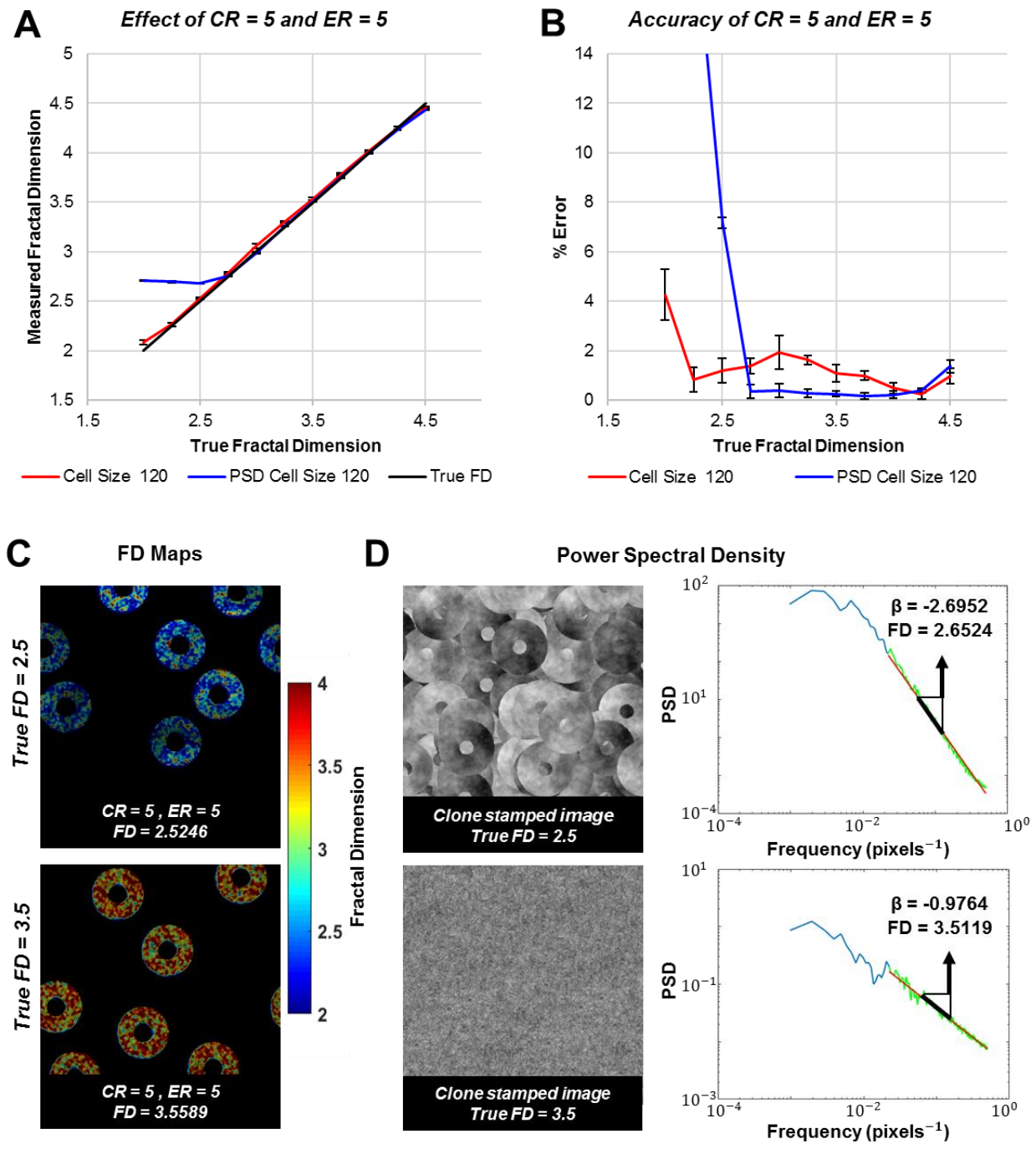

Figure 2.3. Comparison of the accuracy of the MBM and PSD analysis of simulated images (120 pixel diameter cells). **(A)** The MBM (red) is accurate over a larger range of FD values than PSD analysis (blue). **(B)** Mean error in PSD analysis is significantly higher when FD < 2.75. **(C)** Representative FD maps of cells with FD of 2.5 and 3.5 demonstrate the accuracy of the MBM. **(D)** Representative clone-stamped images and PSD curves indicate the PSD is less accurate for smaller FD values.

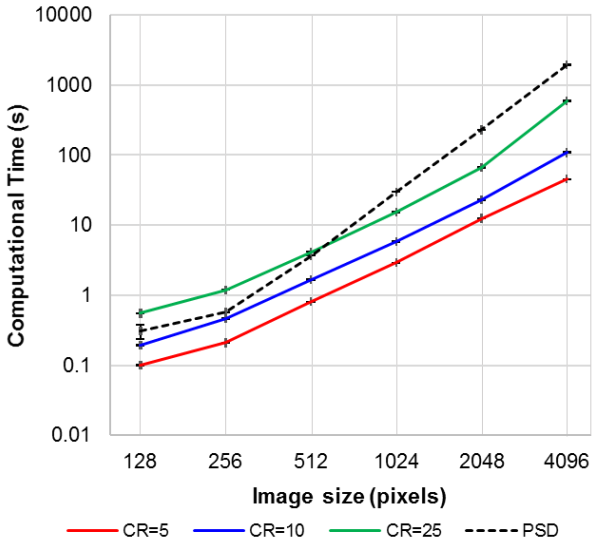

Figure 2.4. Average time required to compute FD through the MBM and PSD analysis on simulated circular cells images for increasing image resolutions of 128 x 128, 256 x 256, 512 x 512, 1024 x 1024, 2048 x 2048, and 4096 x 4096 pixels. An increase in CR from 5 to 25 results in a modest increase in computational time.

2.3.2 Lung Cancer Cells

The MBM revealed a significant change in the mitochondrial FD of radiation-resistant lung cancer cells between 12 and 24 hours after radiation ($p<0.0001$) (Fig. 2.5). Previous work demonstrated that the optical redox ratio of FAD/(NADH+FAD) decreases in the radiation-resistant cell line at 24 hours post-radiation ($p=0.0141$), indicating a shift towards glycolytic metabolism [23], which matches the changes in FD observed here with the MBM. Interestingly, erosion did not produce significant differences in the FD values, despite providing a noticable improvement in the accuarcy of simulated images. While the MBM results matched biochemical changes in cell metabolism observed over time, a change in FD between post-radiation time points was not detectable through the conventional PSD analysis ($p=0.9991$). Unlike the MBM and previous redox ratio measurements [24], PSD analsyis indicated significant differences between parental (control) and radiation-resistant cancer cell lines at every time point (Fig. 2.5c).

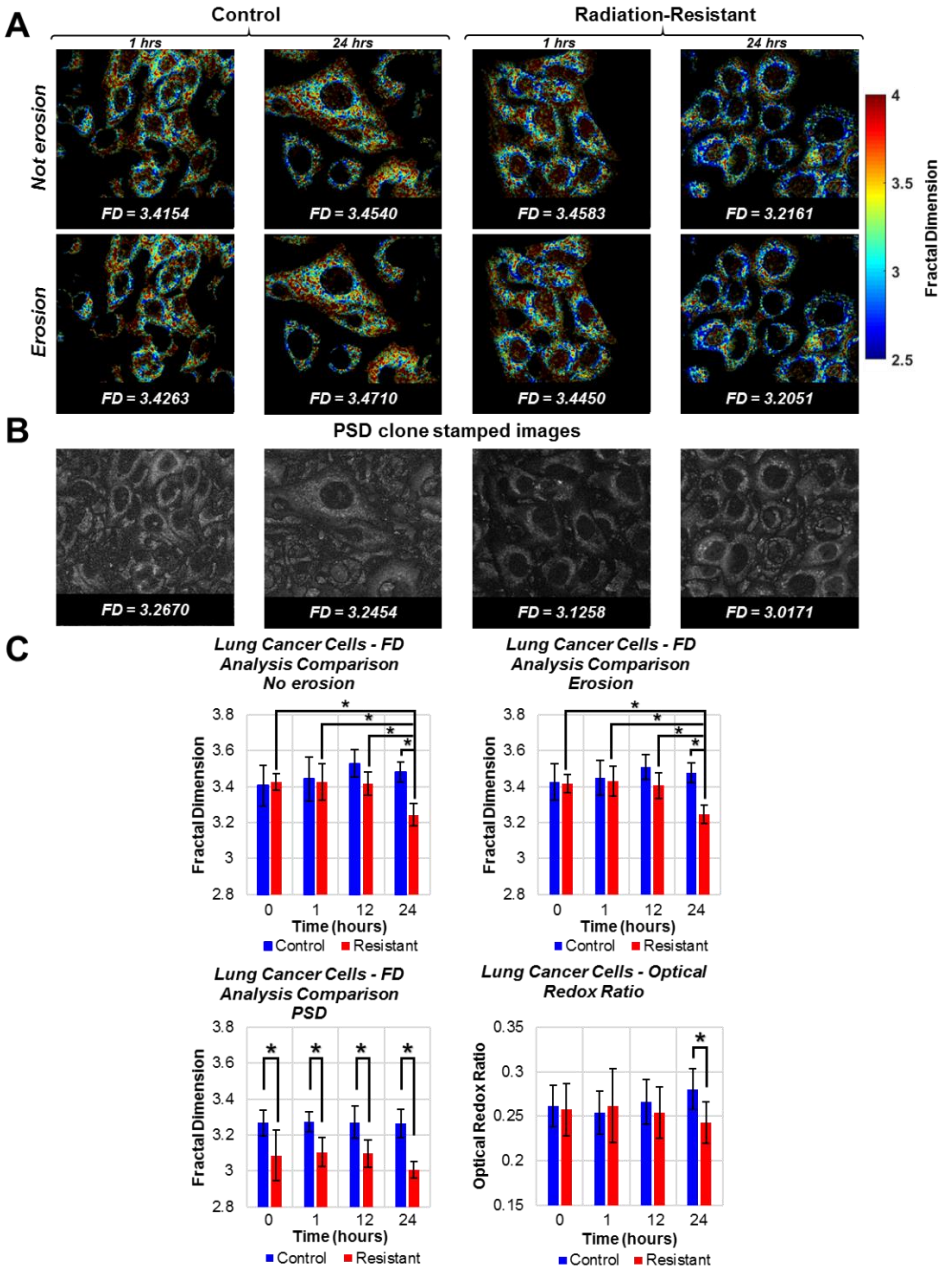

Figure 2.5. Lung Cancer Cells Study **(A)** Representative FD maps corresponding to lung cancer cells of both the control (left) and radiation-resistant (right) group. Top row shows FD maps without erosion and bottom row shows FD maps with erosion. The images were obtained at time periods of 1 and 24 hours post radiation. **(B)** Clone stamped images obtained during the PSD analysis at time periods of 1 and 24 hours as shown in panel (A). **(C)** Summary data demonstrate that the differences of eroding and not eroding the cell objects with the MBM approach are minimal. The MBM method detects significant temporal changes in the mitochondrial organization of radiation resistant cell line at 24 hours, which matches independent measurements of the optical redox ratio of FAD/(NADH+FAD) autofluorescence intensities detailed in [23, 24]. Interestingly, the PSD approach does not reveal the temporal changes detected using the optical redox ratio and MBM.

2.4 Discussion

Our study demonstrates that the MBM is capable of rapidly and accurately quantifying FD within individual cells. By computing local changes in intensity gradients at different image resolutions, the MBM can obtain fractal dimension values from the power law exponent relating surface area and pixel size [8]. Cell simulations demonstrated that the MBM yields accurate FD measurements over a wide range of FD values (2.00-4.50). In addition, the improved accuracy of the MPM relative to PSD analysis, allowed for the detection of structural changes in parental and radiation-resistant A549 cell mitochondria over time, which was supported by previous optical redox ratio measurements that suggested a shift in cellular metabolism [23, 24] (Fig. 2.5c).

Compared to PSD analysis, the MBM offers accuracy over a greater range of FD in biomedical images. Cell simulations using the PSD method resulted in inaccurate FD approximations for FD<2.75 (Fig. 2.3a) with a high maximum error of 19.9% (Fig. 2.3b). This reduced accuracy for the PSD approach is caused by the susceptibility of the method to scale-dependent image features (i.e. cell boundaries). We employed a technique proposed by Xylas et. al. [8] to minimize the effect of scale-dependent features by replicating cellular patterns in the background of the image through clone stamping. However, Xylas et al. and the current study demonstrate that this pre-processing step cannot recover FD values below 2.5 when using PSD analysis. At lower FD values, the image intensity patterns vary over lengths that can approach or exceed the size of the cell, resulting in cell boundaries visible in the clone-stamped images (Fig. 2.3d). These cell boundaries were also visible in experimentally-derived clone-stamped images (Fig. 2.5b) as well, suggesting possibly inaccurate measures of fractal dimension through the PSD. The MBM does not demonstrate this same sensitivity to cell boundaries in experimentally-

derived images (Fig. 2.5a), regardless of whether pixels at the edge of the cell are removed through erosion prior to calculating average values.

The effects of cell or object boundaries can be still observed in the MBM-derived FD maps of the simulated images. However, compared to the PSD, the MBM's edge-effects are limited to the relatively small number of pixels at the boundary of cell objects (Fig. 2.2e). Increasing the size on the convolution disk can increase the number of pixels affected by these large (non-fractal) changes in intensity (e.g. cell or nuclei borders). To overcome the consequences of these artifacts, erosion of the cell mask using the same kernel size as that used during convolution yielded more accurate average FD values in simulated images (Fig. 2.2e). The erosion procedure thins the cell mask by a specific number of pixels and enables computation of an average FD value from only unaffected pixels within the cell or region of interest. In general, the simulations revealed that using the MBM with equal CR and ER size yields a better FD approximation. However, erosion did not have a large impact in the average FD value when it was performed on the A549 cell images (Fig. 2.5). This might be related to the more gradual intensity change between cell and background regions within actual biomedical images. It is important to highlight that although cell boundaries can influence the MBM in some cases, they are not as sensitive to the final FD measurement as they are when using the PSD approach.

The MBM offers improvements in accuracy and speed relative to PSD analysis of mitochondrial clustering, but the primary advantage of the MBM is the ability to report FD on a pixel-by-pixel basis. Given that single cell assessments of mitochondrial function are possible using time-resolved and intensity-based NADH and FAD autofluorescence imaging [14, 25], the ability to also assess rapidly mitochondrial structure on a cell-by-cell basis can enable

complementary information to assess disease and repair [18]. Fractal analysis has been employed in a number of biomedical applications beyond mitochondrial clustering, including the characterization of electroencephalogram (EEG) signals [26], the morphology of the brain in MRI images [27], and the anisotropy degree of bone structures [28]. The MBM may be particularly useful in detecting changes in vasculature surrounding tumors produced by aberrant angiogenesis [29]. Changes in extracellular matrix organization in different disease or repair states may also offer new applications for this method capable of rapidly measuring regional differences in structural organization. In summary, the modified blanket method for computing fractal dimension offers a unique ability to rapidly map out changes in local image patterns for a variety of biomedical applications beyond mitochondrial organization.

2.5 Funding

National Institutes of Health (NIH R00EB017723, NIH R01AG056560); Arkansas Biosciences Institute; NIGMS P20GM103625; and the Jean Ostermeier Memorial Cancer Research Endowed Award.

2.6 Acknowledgements

NIH R00EB017723 (KPQ), NIH R01AG056560 (KPQ), Arkansas Biosciences Institute (KPQ, NR), NIGMS P20GM103625 (RPMD), and the Jean Ostermeier Memorial Cancer Research Endowed Award (IV).

2.7 Disclosure

The authors declare that there are no conflicts of interest related to this article.

2.8 References

1. J. Li, Q. Du, and C. Sun, “An improved box-counting method for image fractal dimension estimation,” Pattern Recognition **42**(11) 2460-2469 (2009).

2. J.B. Bassingthwaighte, R.B. King, and S.A. Roger, “Fractal Nature of Regional Myocardial Blood Flow Heterogeneity,” Circ. Res. **65**(3) 578-590 (1989).

3. J.H. Brown, V.K. Gupta, B.L. Li, B.T. Milne, C.R., and G.B. West. “The fractal nature of nature: power laws, ecological complexity and biodiversity,” Philos. Trans. R. Soc. Lond. B. Biol. Sci. **357**(1421) 619–626 (2002).

4. D. Pouli, M. Balu, C.A. Alonzo, Z. Liu, K.P. Quinn, F. Rius-Diaz, R.M. Harris, K.M. Kelly, B.J. Tromberg, and I. Georgakoudi, “Imaging mitochondrial dynamics in human skin reveals depth-dependent hypoxia and malignant potential for diagnosis,” Sci. Transl. Med. **8**(367), 367-388 (2016).

5. A.A. Dukes, V.S. Van Laar, M. Cascio, and T.G. Hastings, “Changes in endoplasmic reticulum stress proteins and aldolase A in cells exposed to dopamine,” Journal of Neurochemistry **106**(1) 333–346 (2008).

6. K.P. Quinn, G.V. Sridharan, R.S. Hayden, D.L. Kaplan, K. Lee, and I. Georgakoudi, “Quantitative metabolic imaging using endogenous fluorescence to detect stem cell differentiation,” Sci. Rep. **3**(3432) (2013).

7. D.H. MacDonald, M. Hunter, K.P. Quinn, and I. Georgakoudi, “Autocorrelation method for fractal analysis in nonrectangular image domains,” Opt. Lett. **38**(21) 4477-4479 (2013).

8. J. Xylas, K.P. Quinn, M.Hunter, and I. Georgakoudi, “Improved Fourier-based characterization of intracellular fractal features,” Opt. Express **20**(21) 23442-23455 (2012).

9. S.B. Berman, and T.G. Hastings, “Dopamine oxidation alters mitochondrial respiration and induces permeability transition in brain mitochondria: implications for Parkinson's disease,” J. Neurochem. **73**(3) 1127-1137 (1999).

10. J. Xylas, A. Varone, K.P. Quinn, D. Pouli, M.E. McLaughlin-Drubin, H.T. Thieu, M.L. Garcia-Moliner, M. House, M. Hunter, K. Munger, and I. Georgakoudi, “Noninvasive assessment of mitochondrial organization in three-dimensional tissues reveals changes associated with cancer development,” Int. J. Cancer **136**(2) 322–332 (2015).

11. C.B Caldwell, S.J. Stapleton, D.E. Holdsworth, R.A. Jong, W.J. Weiser, G. Cooke, and M.J Yaffe, “Characterization of mammographic parenchymal pattern by fractal dimension,” Phys. Med. Biol. **35**(2) 235-247 (1990).

12. T.M. Cabral and R.M. Rangayyan, Fractal Analysis of Breast Masses in Mammograms (Morgan & Claypool Publishers, 2012).

13. R.M. Rangayyan and T.M. Nguyen, "Fractal Analysis of Contours of Breast Masses in Mammograms," J. Digit. Imaging **20**(3) 223-237 (2007).

14. I. Georgakoudi and K.P. Quinn, "Optical Imaging Using Endogenous Contrast to Assess Metabolic State," Annu. Rev. Biomed. Eng. **14** 351-367 (2012).

15. D. Pendin, R. Filadi, and P. Pizzo, "The Concerted Action of Mitochondrial Dynamics and Positioning: New Characters in Cancer Onset and Progression," Front Oncol. **7**(102) (2017).

16. F. Bartolomé and A.Y. Abramov, "Measurement of mitochondrial NADH and FAD Autofluorescence in Live Cells," in Mitochondrial Medicine Methods in Molecular Biology, V. Weissig and M. Edeas, eds. (Humana Press, 2015).

17. K. Foroutan-pour, P. Dutilleul, and D.L. Smith, "Advances in the implementation of the box-counting method of fractal dimension estimation," Applied Mathematics and Computation **105**(2) 195-210 (1999).

18. Z. Liu, D. Pouli, C. A. Alonzo, A. Varone, S. Karaliota, K.P. Quinn, K. Münger, K. P. Karalis, and I. Georgakoudi, "Mapping metabolic changes by noninvasive, multiparametric, high-resolution imaging using endogenous contrast," Sci. Adv. **4**(3) (2018).

19. J.W. Byng, N.F. Boyd, E. Fishell, R.A. Jong, and M.J. Yaffe, "Automated analysis of mammographic densities," Phys. Med. Biol. **41**(5) 909-923 (1996).

20. M. P. Paskaš, I. S. Reljin, and B. D. Reljin, "Multifractal Framework Based on Blanket Method," The Scientific World Journal **28**.

21. S. Peleg, J. Naor, R. Hartley, and D. Avnir, "Multiple Resolution Texture Analysis and Classification," IEEE Transactions on Pattern Analysis and Machine Intelligence **PAMI-6**(4) 518-523 (1984).

22. D.Chappard, A.Chennebault, M.Moreau, E.Legrand, M.Audran, and M.F.Basle, "Texture analysis of X-ray radiographs is a more reliable descriptor of bone loss than mineral content in a rat model of localized disuse induced by the Clostridium botulinum toxin," Bone **28**(1) 72-79 (2001).

23. K. Alhallak, S.V. Jenkins, D.E Lee, N.P. Greene, K.P. Quinn, R.J. Griffin, R.P.M Dings, and N. Rajaram, "Optical imaging of radiation-induced metabolic changes in radiation-sensitive and resistant cancer cells," J. Biomed. Opt. **22**(6), 060502 (2017).

24. D.E. Lee, K. Alhallak, S.V. Jenkins, I. Vargas, N.P. Greene, K.P. Quinn, R.J. Griffin, R.P.M. Dings, and N. Rajaram, "A Radiosensitizing Inhibitor of HIF-1 alters the Optical Redox State of Human Lung Cancer Cells In Vitro," Sci. Rep. **8**(8815) (2018).

25. O. I. Kolenc and K.P. Quinn, "Evaluating Cell Metabolism Through Autofluorescence Imaging of NAD(P)H and FAD," Antioxid Redox Signal (2018).

26. W.Y. Hsu, C.C. Lin, M.S. Ju, and Y.N. Sun, "Wavelet-based fractal features with active segment selection: Application to single-trial EEG data," Journal of Neuroscience Methods **163**(1) 145-160 (2007).

27. J.M. Zook, and K.M. Iftekharuddin, "Statistical analysis of fractal-based brain tumor detection algorithms," Magnetic Resonance Imaging **23**(5) 671-678 (2005).

28. R. Jennane, R. Harba, G. Lemineur, S. Bretteil, A. Estrade, and C.L. Benhamou, "Estimation of the 3D self-similarity parameter of trabecular bone from its 2D projection," Medical Image Analysis **11**(1) 91-98 (2007).

29. C.E. Priebe, J.L. Solka, R.A. Lorey, G.W. Rogers, W.L. Poston, M. Kallergi, W. Oian, L.P. Clarke, and R.A. Clark, "The application of fractal to mammographic tissue classification," Cancer Letters **77**(2) 183-189 (1994).

CHAPTER 3

A QUANTITATIVE APPROACH TO ASSESS THE RELATIONSHIPS AMONG ACTIN AND MITOCHONDRIAL ORGANIZATION

Abstract

Multiple pathological conditions are known to present subcellular abnormalities. Unfortunately, many subcellular structural characteristics are difficult to quantify, because standard image processing techniques require multiple user inputs to segment, denoise, and measure structural features. A versatile set of automated techniques developed to assess the organization of actin and mitochondria through measurements of fractal dimension, fiber orientation, and directional variance is introduced. We combined these techniques with other computational methods to also quantify changes in nuclear elongation through the nuclear aspect ratio. In addition, these techniques can be executed simultaneously at different length scales and on a pixel-by-pixel basis, without any kind of image pre-processing or segmentation. We apply these tools to quantify changes in organelle dynamics of mice fibroblasts (NIH 3T3), specifically those corresponding to actin, mitochondria, and nuclei after being treated with L-buthionine-sulfoximine (BSO) at increasing concentrations for a period of 24 hours. We validate that BSO treatment produces oxidative stress and a variety of changes to the mitochondria and actin. Specifically, we demonstrate that the orientation and fractal organization of actin and mitochondria are highly affected by BSO, and there are strong correlations among these measurements of subcellular features.

3.1 Introduction

Cellular organization and dynamics have proven to be of major significance in understanding the complexity of a variety of biological mechanisms [1]. It has been demonstrated

that cells have the capacity to react to certain stimuli and adapt accordingly to meet the needs of the organism [2, 3]. Processes such as the transmission of signals via proteins [4], cell to cell communication [5], and the interaction with the extracellular matrix (ECM) [5], stimulate cells to continuously undergo a variety of chemical and physical changes. Within cells, organelles and other cellular structures are responsible for controlling key reactions and carrying on responses that ultimately decide the fate of the cell and tissue physiology [6]. Conditions such as cancer [7], heart disease [8], myopathy [9], Leigh syndrome [10], Alzheimer's [11], and several others arise when dysfunction in the actin cytoskeleton, mitochondria, or other organelles produce structural and functional changes.

With modern advances in imaging techniques involving immuno-specific fluorescent dyes, we are now able to observe the structural dynamics within individual cells. Numerous recent studies have used fluorescence microscopy to characterize certain cellular properties, observing the reaction resulting from interactions with specific mediums/treatments, the relationship of some cellular characteristics to a particular disease, and the differences among cell lines. For instance, using a phalloidin-based marker, previous studies have labeled and observed F-actin, a main component of the cytoskeleton, to find its relationship to dendritic spine loss [12] and to classify changes in rat basophilic leukemia (RBL) cells following bisdemethoxycurcumin (BDCM) treatment [13]. In addition, some cancer studies have reported using Mitotracker, a fluorescent dye that labels mitochondria, to measure mitochondrial density in pancreatic cells [14], to classify mitochondrial shapes in different breast cancer cells [15], and to evaluate the efficacy of synthetic antioxidants in primary striatal neuronal cultures obtained from mice models of Huntington disease [16]. The development of image analysis techniques has provided quantitative information on observed changes in mitochondrial networks [17-19], actin orientation [20], and nuclei shape [21],

which have been critical in the understanding of certain cellular responses and pathological conditions. However, the vast majority of current analysis techniques lack the ability to rapidly assess organelle organization and orientation within individual cells without significant user input and feature segmentation. As a result, a quantitative understanding of the relationships between the cytoskeleton and mitochondria is not well understood.

We have recently developed two distinct image analysis techniques capable of quantifying fractal dimension and fiber orientation over different length scales within biomedical images without the need for subcellular feature segmentation. These tools were developed to automatically obtain information relevant to structure morphology and organization by providing accurate measurements of fractal dimension (FD) [22], fiber orientation (FO) [23] and fiber directional variance (DV) [24] within a user-specified length-scale. These analysis methods have been successfully applied to autofluorescence images of mitochondria [22] and assessments of collagen fiber orientation in tissue histology [24], but have not been combined to understand relationships among subcellular features in triple-labelled fluorescence microscopy images. Here we demonstrate with the development and integration of these tools, we are able to quantitatively investigate the interactions and dynamics of cellular components, specifically those occurring in the cytoskeleton (F-actin), the mitochondria, and the cell nuclei. In order to induce abrupt cellular changes and demonstrate the utility of our techniques, we applied treatments of L-buthionine-sulfoximine (BSO) to mouse fibroblasts (NIH 3T3) during 24 hours in culture medium. In previous studies, BSO has been used to impair the production of glutathione (GSH), an antioxidant that plays a critical role in preventing damage by reactive oxygen species. Depletions of GSH have been linked to delays in wound healing [25], oxidative stress [26], the manifestation of dense cataracts [27], and the depolymerization of actin-binding proteins in the cytoskeleton [28]. Our set

of analysis techniques demonstrated a dose-dependent sensitivity to changes in the organization and orientation of F-actin and mitochondria, as well as nuclear shape following BSO treatment. Our analysis toolset also enabled us to characterize strong associations between different subcellular features during dynamic changes in cell morphology as oxidative stress increased within cells.

3.2 Results

3.2.1 Cell viability and oxidative stress

BSO treatment induces a dose-dependent increase in oxidative stress

To understand the effects of BSO treatment on fibroblasts, cell viability and oxidative stress were first assessed. Mice fibroblasts (NIH 3T3) were incubated for 24 hours in media with BSO concentrations of 0, 2.5, 5, or 12.5 mM. Following this, the cells were stained with Calcein-AM and Ethidium homodimer-1 (EthD1) to quantify live and dead cells respectively. Images of Calcein-AM (green) and EthD1 (red) obtained through confocal microscopy showed a clear increase in the number of dead cells at higher BSO concentrations (Fig. 3.1A) as well as cells with disrupted plasma membranes (Fig. 3.1B (a-d)). At low BSO concentrations (2.5mM), the average percentage of live cells (91.2±4.43%) was somewhat similar to untreated controls (97.4±3.5%). However, at higher treatment concentrations, this percentage decreased significantly to 77.4±11.3% at 5mM and 53.6±12.1% at 12.5mM) (Fig. 3.1C (top)) ($p<0.0001$). To assess oxidative stress, MitoSOX staining was also performed and measured by computing the average intensity of image fields at each treatment concentration. Cells treated with BSO demonstrated a clearly stronger signal from MitoSOX ($p<0.0001$) than controls (Fig. 3.1B, C), suggesting a linear increase in mitochondrial oxidative stress following increasing BSO treatment.

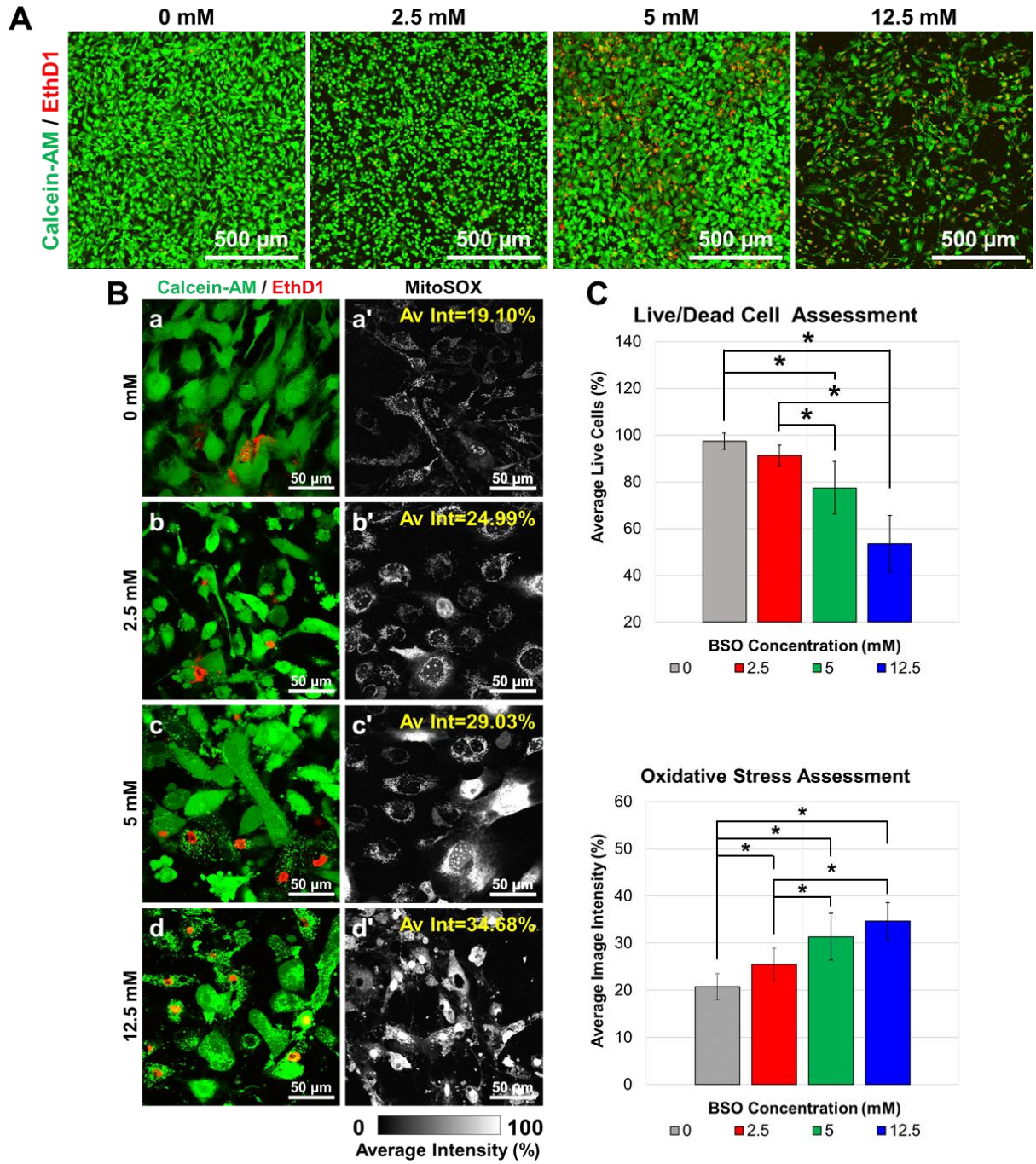

Figure 3.1. Assessment live/dead cell viability and oxidative stress of NIH 3T3s treated with BSO at 0, 2.5, 5, and 12.5 mM for 24 hours. Representative laser scanning confocal images acquired at 20x showing live and dead cells detected with Calcein-AM (staining the cytoplasm) and EthD1 (staining the cell nuclei) respectively (**A**). Image fields acquired at 60x after BSO treatment (**B**). Field composites of Calcein-AM and EthD1 (**a-d**). MitoSOX intensity images acquired at similar laser power and sensitivity representing oxidative stress as measured by the differences in image intensity (**a'-d'**). Average percentage of live cells (top) and oxidative stress (bottom) at different BSO treatments (**C**).

3.2.2 Fractal Dimension and Directional Variance

Fractal dimension and directional variance change in response to BSO treatment

After confirmation of the induction of oxidative stress via BSO treatment, fluorescent labeling of F-actin, mitochondria, and cell nuclei was performed at concentrations of 0, 2.5, 5, and 12.5 mM (n=6 dishes per dose). Changes in fractal dimension (FD) were measured from both the F-actin and mitochondria fluorescence images on a pixel by pixel basis using established automated computational techniques in MATLAB [22]. FD values can be interpreted as inversely related to the level of organelle clustering. Additionally, an orientation vector summation algorithm was used to detect fiber orientation (FO) at each pixel [23], and directional variance (DV) within a 25-pixel radius was computed to assess the strength of feature alignment [23, 24] in the mean orientation direction. These analysis techniques revealed significant variations in both FD and DV for actin and mitochondria (Fig. 3.2 and Fig. 3.3).

Treatment with BSO resulted in clear alterations in cellular morphology and actin filament organization (Fig. 3.2A). A decrease in FD measurements following BSO treatment reflected high levels of actin clustering, with significant differences between the control and BSO treatments at 2.5mM ($p=0.0230$), 5mM ($p=0.0023$), and 12.5mM ($p=0.0006$) (Fig. 3.2B). In addition, orientation of actin filaments was considerably altered after BSO treatments, presenting less consistency in actin fiber direction within each cell when compared to the control (Fig. 3.2A). As a result, actin fiber DV maps showed a linear increase with increasing BSO concentration resulting in significant differences between control and 5mM ($p=0.0172$), control and 12.5mM ($p=0.0002$), and 2.5mM and 12.5mM ($p=0.0052$).

BSO treatment had smaller effects on the FD and DV of mitochondria (Fig. 3.3). Although cell morphology differed with BSO treatment, the size of mitochondria did not (Fig. 3.3 (a-d, a'-

d’’)). As a result, only a minor decrease in FD following BSO treatment (Fig. 3.3 (a’’-d’’)) was observed with no statistically significant differences (Fig. 3.3B). Although orientation of mitochondria was more random than the actin (Fig. 3.3A (a’’’-d’’’)), DV maps demonstrated that mitochondria became less aligned after BSO treatment (Fig. 3.3A (a’’’’-d’’’’)), which produced significantly higher values at concentrations of 5mM ($p=0.0339$) and 12.5mM ($p=0.0011$) relative to untreated controls.

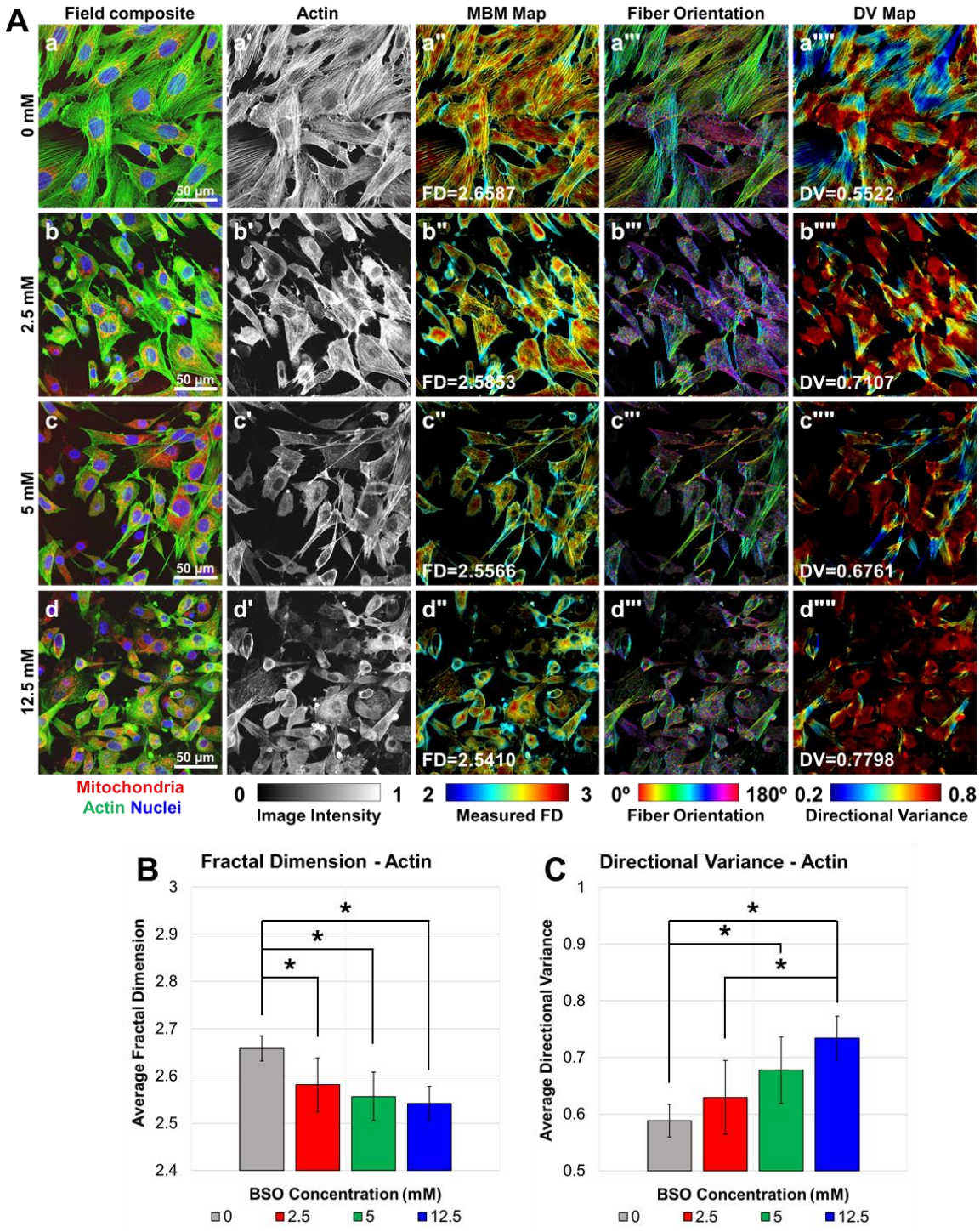

Figure 3.2. Laser confocal imaging of actin (Phalloidin) in NIH 3T3 cells treated with BSO at 0, 2.5, 5, and 12.5 mM for 24 hours. Representative 60x averaged z-stack images showing the substantial depolymerization of F-actin caused by depletions of GSH levels (**A**)**.** Field composites of Mitotracker Red, Phalloidin and NucBlue (**a-d**). Phalloidin signal representing F-actin (**a'-d'**). Resulting MBM maps (**a"-d"**), Fiber orientation maps (**a"'-d"'**), and DV maps (**a""-d""**) of actin. Average FD **(B)** and DV (**C**) bar graphs.

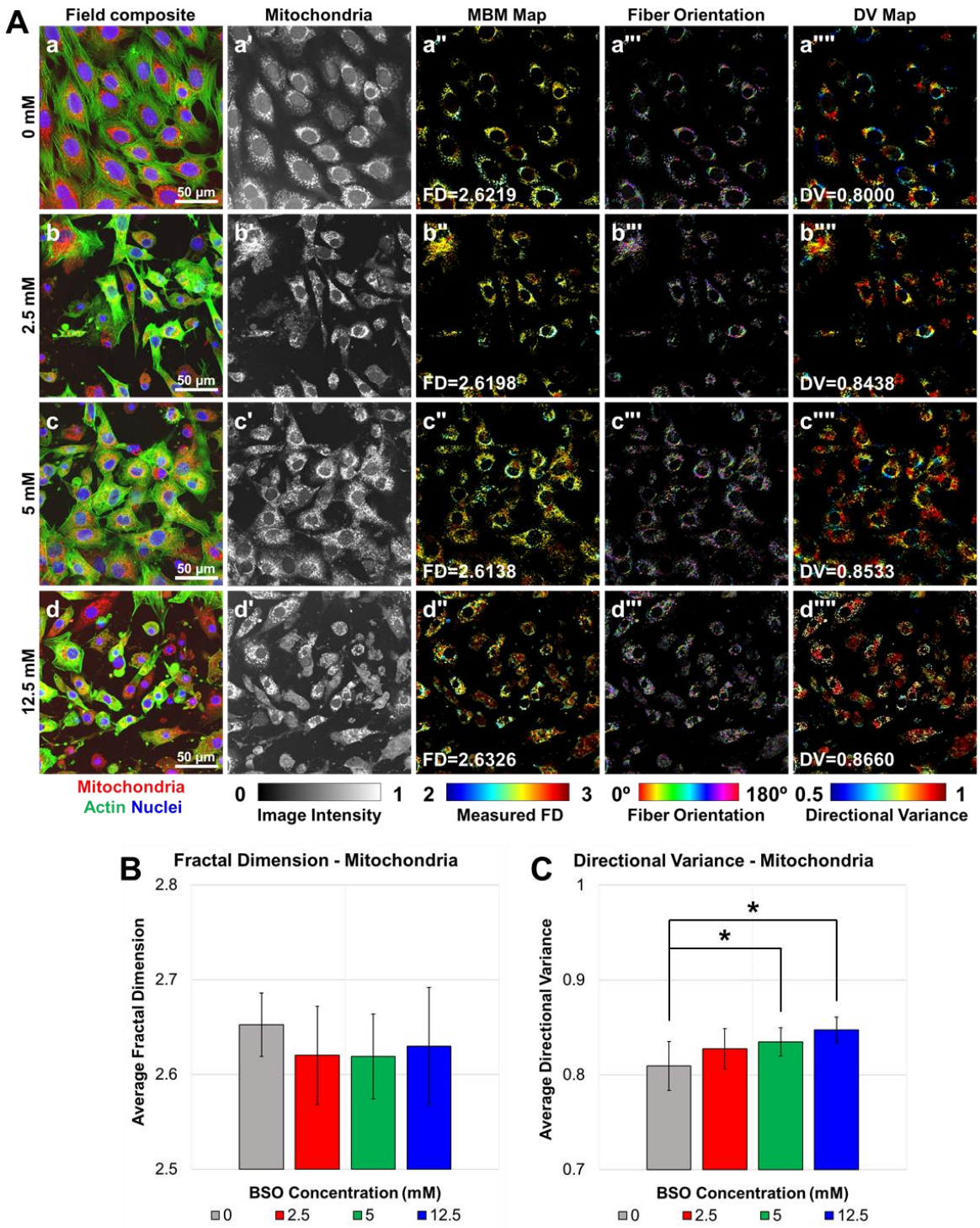

Figure 3.3. Laser confocal imaging of mitochondria (Mitotracker Red) in NIH 3T3 cells treated with BSO at 0, 2.5, 5, and 12.5 mM for 24 hours. Representative 60x averaged z-stack images showing the reorganization of mitochondria due to cellular stress (**A**)**.** Field composites of Mitotracker Red, Phalloidin and NucBlue (**a-d**). Mitotracker Red signal representing mitochondria (**a'-d'**). Resulting MBM maps (**a"-d"**), Fiber orientation maps (**a"'-d"'**), and DV maps (**a""-d""**) of mitochondria. Average FD **(B)** and DV (**C**) bar graphs.

3.2.3 Nuclear Aspect Ratio

Nuclear Aspect Ratio (NAR) decreases in response to BSO treatment

BSO treatment also caused a change in the shape of the nucleus. To quantify these changes, each nucleus within an image field was approximated as an ellipse. Using the regionprops function in MATLAB, the size of the major and minor axis (in pixels) of each ellipse was measured. Average NAR was then calculated based on the total number of cells per image field. Following BSO treatment, the cells presented a smaller cell nucleus cross-section that could be related to a change in nuclear shape or size (Fig. 3.4A (a-d, a'-d'). Nuclear aspect ratio maps showed the nucleus of many cells becoming less elongated after treatment (Fig. 3.4A (a''-d'')), resulting in a significant decrease in nuclear aspect ratio at BSO concentrations of 5mM ($p=0.0336$) and 12.5mM ($p=0.0013$) relative to untreated controls (Fig. 3.4B).

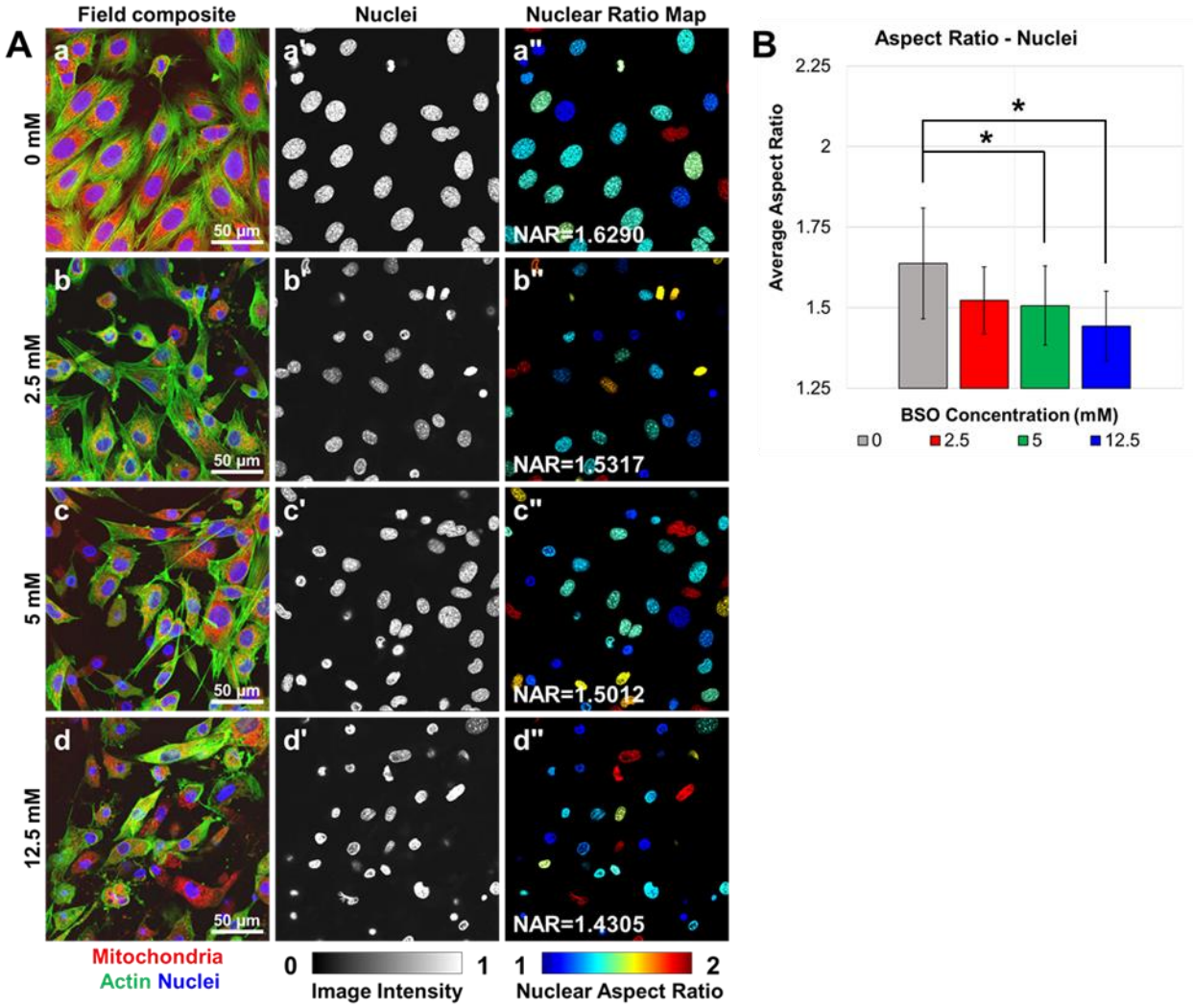

Figure 3.4. Laser confocal imaging of nuclei (NucBlue) in NIH 3T3 cells treated with BSO at 0, 2.5, 5, and 12.5 mM for 24 hours. Representative 60x averaged z-stack images showing the morphological changes of cell nuclei caused by a depolymerized cytoplasm (**A**)**.** Field composites of Mitotracker Red, Phalloidin and NucBlue (**a-d**). NucBlue signal representing nuclei (**a'-d'**). Resulting Nuclear Aspect Ratio maps (**a"-d"**). Average Aspect Ratio bar graph **(B**).

3.2.4 Correlations

Correlations among subcellular features demonstrates interconnected behavior in response to BSO treatment

Correlations Significant correlations among FD, DV, and NAR were identified from the images of actin, mitochondria, and cell nuclei (Table 3.1). Nuclear aspect ratio was significantly correlated with mitochondria (FD and DV) as well as actin (FD and DV) changes (Table 1). Among the strongest relationships, there was a negative correlation between nuclear aspect ratio and actin DV ($R=-0.533$, $p<0.0001$) (Fig. 3.5). There also were strong positive correlations between mitochondria DV and actin DV ($R=0.5038$, $p<0.0001$), as well as between actin FD and mitochondria FD ($R=0.443$, $p<0.0001$) (Fig. 3.5). Actin FD and mitochondria DV ($R=-0.3633$, $p<0.0001$) also were weakly correlated. Interestingly, measurements of actin (FD and DV) were correlated with each other ($R=-0.5891$, $p<0.0001$), while measurements of mitochondria (FD and DV) were not ($R=-0.086$, $p=0.1899$).

Structural feature	Structural feature	Correlation	p-value
Actin FD	Actin DV	-0.5891	<.0001
Nuclear Aspect Ratio	Actin DV	-0.533	<.0001
Mitochondria DV	Actin DV	0.5038	<.0001
Actin FD	Mitochondria FD	0.443	<.0001
Nuclear Aspect Ratio	Actin FD	0.3883	<.0001
Actin FD	Mitochondria DV	-0.3633	<.0001
Nuclear Aspect Ratio	Mitochondria DV	-0.2822	<.0001
Mitochondria FD	Actin DV	-0.1519	0.0201
Mitochondria FD	Mitochondria DV	-0.086	0.1899
Nuclear Aspect Ratio	Mitochondria FD	0.0477	0.4673

Table 3.1. Correlation table of cell structure measurements. Table showing the correlation of FD, DV, and NAR measurements between the stained cellular structures (mitochondria, actin, and cell nuclei).

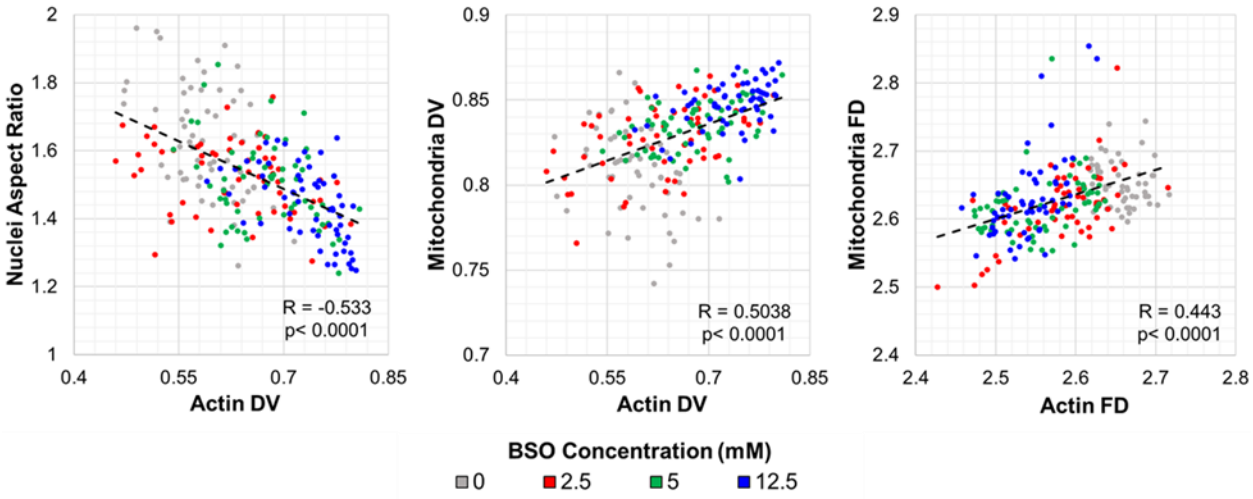

Figure 3.5. Correlation scatterplots of structural features showing the relationship among measurements of FD, DV and NAR of NIH 3T3 cells in response to BSO treatments at 0, 2.5, 5, and 12.5 mM.

3.3 Discussion

Our study demonstrates that the set of automated techniques we developed is capable of simultaneously quantifying structural changes in alignment and organization of both the mitochondria and the actin cytoskeleton (Fig. 3.2 & Fig. 3.3), which correlated with changes in the elongation of the cell nuclei (Fig. 3.4). Furthermore, we also demonstrated that values of FD and DV in both the actin and mitochondria were closely correlated with each other, providing a quantitative measure of the relationship between the cytoskeleton and mitochondrial network following exposure to a cellular stressor such as BSO (Fig. 3.5). Many of these changes (Fig. 3.2-3.3) occurred in a dose-dependent manner that matched the level of oxidative stress (Fig. 3.1), suggesting our toolset may provide a sensitive approach to quantifying the structural changes resulting from other pathological conditions that are associated with oxidative damage, such as diabetes [29, 30], cancer [31, 32], Alzheimer's [33, 34], Parkinson's [35, 36], and cardiovascular disease [37].

Glutathione (GSH) is the most abundant thiol molecule synthesized by cells [38, 39], and as an antioxidant, its main role is to neutralize xenobiotic compounds and reactive species, thus preventing oxidative damage [38]. However, GSH is also involved in multiple cellular dynamics that play a key role in maintaining the cell cycle. For instance, a decline in the homeostatic levels of GSH can promote mitochondrial ROS, impairing bioenergetics and encouraging mitochondrial permeability transition pore (mPTP) opening, which is crucial for cell death in both apoptosis and necrosis [40]. In addition, GSH also monitors cellular division in the cell nucleus [41] and modulates multiple signaling cascades [40]. Although GSH has been widely studied in the past, few experiments have been performed to address and quantify the morphological effects of reducing the abundance of such a molecule in mammalian cells. Using BSO as a GSH depletion drug in our experiments, we were able to validate that lowering the GSH levels of cells such as fibroblasts not only disrupts homeostasis and cell morphology, but also affects the morphology of multiple subcellular structures (Fig. 3.2-3.4).

Similar to our study, previous work has reported the use of BSO in inducing changes in cellular dynamics. For instance, BSO has been applied to decrease the levels of GSH in MSN neuroblastoma cells, leading to the depolymerization of the cytoskeleton [28]. In that study, GSH levels were depleted 70% compared to the control while preventing oxidative stress. As a result, the expression of actin binding proteins decreased, leading to morphological changes in the cytoskeleton. Similar findings were also reported in a study exploring the relationship of actin glutathionylation and cell spreading [42]. We complemented these observations by quantifying the changes in the alignment and organization of the cytoskeleton through DV and FD measurements of actin following similar BSO treatments (Fig. 3.2). We showed that the depletion of GSH through increasing BSO concentrations disrupts the shape of the cells, increasing the clustering and the

directional variance of the cytoskeleton as shown by the dynamic changes in actin filament organization (Fig. 3.2). Oxidative stress has also been reported to be linked to the depletion of GSH [26, 28] and the presence of mitochondria superoxide and other reactive species [43, 44]. BSO treatments produced an increase in mitochondrial oxidative stress (Fig. 3.1B,C), which also coincided with an increase in mitochondrial directional variance, suggesting more of a punctate organization (Fig. 3.3), which has been reported to occur in oxidative stress conditions [33, 45].

Quantitative assessments of the organization of certain subcellular structures have been previously explored. For example, Fourier-based techniques have been widely used in the quantification of actin fiber orientation [46, 47]. Although these techniques proved to be sufficient to approximate changes in fiber alignment, they tend to be highly influenced by edge effects and secondary methods of thresholding. Other techniques have also been employed to quantify the mitochondrial organization. For example, skeletonization has been used in the past to measure the dynamics and branching of mitochondrial filaments following the introduction of external agents [48, 49]. In addition, computational techniques such as box counting [50] and power spectral density [51] have been employed to understand the behavior of mitochondria in multiple scenarios. Similar to Fourier-based techniques, these methods require extra steps of image processing, segmentation, and de-noising prior to the actual quantification, making them unsuitable for the analysis of large data sets or images with inherently low signal-to-noise ratios, such as autofluorescence imaging [22, 52]. In comparison, our techniques do not require pre-processing of any kind and can be applied at different length scales of spatial resolution on a pixel-by-pixel basis without thresholding or segmentation. In addition, our methods proved to be accurate and sensitive to changes in the organization of both actin and mitochondria. More importantly, they can quantify both fiber alignment and fractal organization simultaneously, allowing a

comprehensive assessment of organization that can be compared to additional measurements, such as nuclear aspect ratio [46].

Combining both feature clustering and orientation analysis techniques that do not rely on time-consuming pre-processing steps represents a significant advantage in fluorescence microscopy. Since we are now capable of assessing the relationships among actin, mitochondria, nuclei, and potentially other subcellular structures, we can more objectively assess structural dynamics and the relative effects of different cellular perturbations, whether they are chemical, mechanical, internal, or external. Due to the low computational costs and the rapid speed of this analysis, we could also employ these techniques on larger image data sets, such as tissue samples or 3D organoid cultures, in which we could evaluate the heterogeneity of subcellular structures in complex pathological conditions such as diabetes, cancer, or aging. As microscopy techniques continue to generate larger and larger data sets through enhancements in imaging depth, resolution, and speed, these rapid and automated image analysis techniques will be critical in understanding complex biological relationships and disease states.

3.4 Materials and Methods

3.4.1 Cell culture and L-buthionine-sulfoximine (BSO) treatment

Frozen mice fibroblasts (NIH 3T3) were thawed and passaged to 75mL treated cell culture flasks (VWR 10861-646) at a density of 500,000 cells/mL to reach a stable cell growth prior to experimentation. The cells' necessary nutrients were provided in complete media, containing Dulbecco's Modified Eagle Medium (DMEM) (VWR VWRL0101-0500) with 10% Fetal Bovine Serum (FBS) and 1% L-glutamine. Upon reaching confluency, the cells were passaged to 35 mm glass bottom dishes (MatTek Corporation P35G-1.5-10-C) previously treated with human fibronectin (Corning® VWR 47743-654), which promoted cell adhesion and

prevented the cells from detaching after treatment. Cells were seeded at a density of 60,000 cells/mL on each dish and allowed to grow for 24 hours at 37°C. Cells were monitored for accurate confluency prior to treatment after this period of time. BSO (Sigma-Aldrich B2515-1G) was diluted in cold distilled water following the supplier's protocol to create a stock solution. Under sterile conditions, the BSO stock solution was further diluted in complete media to a final volume of 1 mL at 0, 2.5, 5, or 12.5 mM separately. Cells were incubated in BSO media for 24 hours at 37°C.

3.4.2 Cell viability assessment

A live/dead fluorescent staining kit was employed to assure the viability of the cells after BSO treatment. LIVE/DEAD™ Viability/Cytotoxicity Kit (Thermo Fisher Scientific L3224) was used to label live and dead cells. Following the supplier's protocol, live and dead cells were stained with Calcein-AM and Ethidium homodimer-1 (EthD1) respectively. Calcein-AM indicated intracellular esterase activity in green, and EthD1 showed loss of membrane integrity in red. Images of each BSO treatment were acquired using a laser scanning confocal microscope and the average percentage of live cells was calculated.

3.4.3 Oxidative stress assessment

After BSO treatment, cells were washed with complete DMEM and labeled with MitoSOX Red (Thermo Fisher Scientific M36008) following the manufacturer's protocol. MitoSOX labels mitochondria, where it becomes oxidized by superoxide and fluoresces red. Images were acquired on a laser scanning confocal microscope with the same detector sensitivity and laser power, and the average intensity of the acquired images was calculated.

3.4.4 Cellular staining

After being in BSO treatment for 24 hours, the cell culture dishes (n=6 per concentration) were stained with MitoTracker™ Red CMXRos (Thermo Fisher Scientific M7512) and NucBlue™ Live ReadyProbes™ Reagent (Thermo Fisher Scientific R37605), which labeled mitochondria and cell nuclei respectively. The cells were incubated in the staining solutions for 45 minutes at 37°C. The staining solution was then aspirated, and the cells were washed with complete media two times. Following this, the cells were fixed using a warm solution of 3.7% Paraformaldehyde (PFA) (Sigma-Aldrich 158127) in DMEM for 20 minutes at 37°C. The cells were washed three times with phosphate-buffered saline (PBS) (Sigma-Aldrich P4417) to remove any remaining PFA. Afterwards, blocking was performed using a 10% bovine serum albumin (BSA) (VWR 0332) solution in PBS for 1 hour at 37°C. Lastly, actin was labeled with a staining solution containing 1% BSA in PBS and Alexa Fluor™ 488 Phalloidin (Thermo Fisher Scientific A12379). The cells were incubated in the staining solution for 25 minutes at room temperature covered from light. The solution was aspirated and the cells were washed three times with PBS.

3.4.5 Image acquisition via laser scanning confocal microscopy

A laser scanning confocal microscope (Olympus Fluoview FV10i) was used to acquire images with a 60x water immersion objective (NA=1.2). In order to reduce the amount of background and out of focus light, image acquisition was performed using the smallest confocal pinhole size (ø=50 µm). Image size for acquisition was set to 1024x1024 pixels. For the cell viability (Calcein-AM and EthD1) and MitoSOX assessments, live cell imaging (at 5% CO2 and 37°C) was performed. For the triple staining experiment (actin, mitochondria, and nuclei), images were acquired after PFA fixation. Fluorescent excitation of the dyes was achieved using three lasers (405, 473, and 559 nm). Emission was captured through the use of multiple filters.

Fluorescence from Calcein-AM and actin (Phalloidin) was acquired using the 473 nm laser for excitation with a 520 nm filter for emission. Fluorescent signal from EthD1, MitoSOX, and mitochondria (Mitotracker) was obtained with the 559 nm laser for excitation with a 618 nm, a 581 nm, and a 598 nm filter for emission respectively. Lastly, fluorescence from nuclei (NucBlue) was achieved using the 405 nm laser for excitation and a 461 nm filter for emission.

3.4.6 Fractal Dimension

We employed a modified blanket method to assess fractal dimension that was previously developed [22]. Briefly, this technique interprets an intensity image as a topographical map. Both the vertical and horizontal gradients of the intensity image are first computed. Using a disk kernel of user-defined radius, the gradients are convolved multiple times at different image resolutions. Afterwards, they are used to compute local changes in surface area (SA) as a function of pixel size through the power law exponent β [22]. A FD map is then computed at each image pixel location from this relationship as:

$$FD = 2 - \frac{\Delta \log\ (\text{SA})}{\Delta \log\ (\text{pixel size})} = 2 - \beta \qquad (1)$$

Using the FD map, the average FD can be computed by adding the calculated FD values of each individual pixel over a region of interest (ROI) and dividing by the number of pixels within the same ROI.

3.4.7 Fiber Orientation and Directional Variance

Fiber orientation was computed at each pixel using a previously established vector summation technique [23]. To compute fiber orientation, the program identifies variations in image intensity along different vector orientations through each pixel and computes an orientation based on the summation of all vectors weighted by the maximum possible standard deviation of

intensity. Similar to the MBM, fiber orientation was summarized by computing a pixel-wise fiber orientation map. With this map, the x- and y- components of the alignment vector were separated. Using a disk kernel of user-defined radius, these components and a binary mask of the ROI were convolved, resulting in images of the average x- and y- alignment vector components and the local density of ROI pixels [24]. Lastly, directional variance is calculated by normalizing the magnitude of the resultant alignment vector (R) with the local density of ROI pixels (m) as:

$$DV = 1 - \frac{\mathrm{R}}{\mathrm{m}} \qquad (2)$$

Where alignment extends from 0 (completely aligned) to 1 (no favored direction) [24].

3.4.8 Nuclear Aspect Ratio (NAR)

Cell nuclei images were isolated using a binary mask applied through thresholding of the NucBlue staining patterns in MATLAB. Using the function regionprops [46], which measures multiple properties of the binary mask, small image features and non-nuclei artifacts were isolated based on their pixel area. In doing so, features with areas smaller than 350 pixels were automatically removed from NAR calculations. Using the same function, the major and minor axis (in pixels) from the remaining artifacts in the binary mask (cells) were automatically computed. The average nucleari aspect ratio was then calculated as the ratio of the major and minor axes.

3.4.9 Statistical Analysis

FD, DV, and NAR values were obtained from a total of 240 image fields, each containing three different cellular structures (actin, mitochondria, and cell nuclei), from a total of 6 culture dishes per BSO concentration. A one-way ANOVA with image fields nested within dishes was used to quantify differences between BSO treatments for mitochondria, actin, and cell nuclei separately in JMP, and Tukey HSD post hoc tests were used to identify differences among BSO

concentrations. Correlations were performed while considering all BSO concentrations with the null hypothesis that R=0. Significance was set at $\alpha=0.05$ for all assessments.

3.5 References

1. Dikicioglu, D., Rational Design and Methods of Analysis for the Study of Short- and Long-Term Dynamic Responses of Eukaryotic Systems. Methods Mol Biol, 2019. **2049**: p. 315-327.

2. Brooks, A.N., et al., Adaptation of cells to new environments. Wiley Interdiscip Rev Syst Biol Med, 2011. **3**(5): p. 544-61.

3. Giralt, A. and L. Fajas, Editorial: Metabolic Adaptation to Cell Growth and Proliferation in Normal and Pathological Conditions. Front Endocrinol (Lausanne), 2017. **8**: p. 362.

4. Choquet, D. and A. Triller, The dynamic synapse. Neuron, 2013. **80**(3): p. 691-703.

5. Howard, C.M. and T.A. Baudino, Dynamic cell-cell and cell-ECM interactions in the heart. J Mol Cell Cardiol, 2014. **70**: p. 19-26.

6. Satori, C.P., et al., Bioanalysis of eukaryotic organelles. Chem Rev, 2013. **113**(4): p. 2733-811.

7. Batlle, E. and H. Clevers, Cancer stem cells revisited. Nat Med, 2017. **23**(10): p. 1124-1134.

8. Afanasyeva, M., D. Georgakopoulos, and N.R. Rose, Autoimmune myocarditis: cellular mediators of cardiac dysfunction. Autoimmun Rev, 2004. **3**(7-8): p. 476-86.

9. Naik, P.P., A. Birbrair, and S.K. Bhutia, Mitophagy-driven metabolic switch reprograms stem cell fate. Cell Mol Life Sci, 2019. **76**(1): p. 27-43.

10. Iyer, S., et al., Mitochondrial gene therapy improves respiration, biogenesis, and transcription in G11778A Leber's hereditary optic neuropathy and T8993G Leigh's syndrome cells. Hum Gene Ther, 2012. **23**(6): p. 647-57.

11. Onyango, I.G., J. Dennis, and S.M. Khan, Mitochondrial Dysfunction in Alzheimer's Disease and the Rationale for Bioenergetics Based Therapies. Aging Dis, 2016. **7**(2): p. 201-14.

12. Kommaddi, R.P., et al., Abeta mediates F-actin disassembly in dendritic spines leading to cognitive deficits in Alzheimer's disease. J Neurosci, 2018. **38**(5): p. 1085-1099.

13. Fu, M., et al., Inhibitory effects of bisdemethoxycurcumin on mast cell-mediated allergic diseases. Int Immunopharmacol, 2018. **65**: p. 182-189.

14. Guo, Q., Changes in mitochondrial function during EMT induced by TGFbeta-1 in pancreatic cancer. Oncol Lett, 2017. **13**(3): p. 1575-1580.

15. Sarmiento-Salinas, F.L., et al., Breast Cancer Subtypes Present a Differential Production of Reactive Oxygen Species (ROS) and Susceptibility to Antioxidant Treatment. Front Oncol, 2019. **9**: p. 480.

16. Xun, Z., et al., Targeting of XJB-5-131 to mitochondria suppresses oxidative DNA damage and motor decline in a mouse model of Huntington's disease. Cell Rep, 2012. **2**(5): p. 1137-42.

17. Zamponi, N., et al., Mitochondrial network complexity emerges from fission/fusion dynamics. Sci Rep, 2018. **8**(1): p. 363.

18. Xylas, J., et al., Noninvasive assessment of mitochondrial organization in three-dimensional tissues reveals changes associated with cancer development. Int J Cancer, 2015. **136**(2): p. 322-32.

19. Pouli, D., et al., Imaging mitochondrial dynamics in human skin reveals depth-dependent hypoxia and malignant potential for diagnosis. Sci Transl Med, 2016. **8**(367): p. 367ra169.

20. Alioscha-Perez, M., et al., A Robust Actin Filaments Image Analysis Framework. PLoS Comput Biol, 2016. **12**(8): p. e1005063.

21. Guo, Y., et al., An image processing pipeline to detect and segment nuclei in muscle fiber microscopic images. Microsc Res Tech, 2014. **77**(8): p. 547-59.

22. Vargas, I., et al., Rapid quantification of mitochondrial fractal dimension in individual cells. Biomed Opt Express, 2018. **9**(11): p. 5269-5279.

23. Quinn, K.P. and I. Georgakoudi, Rapid quantification of pixel-wise fiber orientation data in micrographs. J Biomed Opt, 2013. **18**(4): p. 046003.

24. Quinn, K.P., et al., An automated image processing method to quantify collagen fibre organization within cutaneous scar tissue. Exp Dermatol, 2015. **24**(1): p. 78-80.

25. Rasik, A.M. and A. Shukla, Antioxidant status in delayed healing type of wounds. Int J Exp Pathol, 2000. **81**(4): p. 257-63.

26. Kopal, C., et al., Effects of topical glutathione treatment in rat ischemic wound model. Ann Plast Surg, 2007. **58**(4): p. 449-55.

27. Calvin, H.I., C. Medvedovsky, and B.V. Worgul, Near-total glutathione depletion and age-specific cataracts induced by buthionine sulfoximine in mice. Science, 1986. **233**(4763): p. 553-5.

28. Zepeta-Flores, N., et al., Glutathione depletion triggers actin cytoskeleton changes via actin-binding proteins. Genet Mol Biol, 2018. **41**(2): p. 475-487.

29. Wei, W., et al., Oxidative stress, diabetes, and diabetic complications. Hemoglobin, 2009. **33**(5): p. 370-7.

30. Rains, J.L. and S.K. Jain, Oxidative stress, insulin signaling, and diabetes. Free Radic Biol Med, 2011. **50**(5): p. 567-75.

31. Andrisic, L., et al., Short overview on metabolomics approach to study pathophysiology of oxidative stress in cancer. Redox Biol, 2018. **14**: p. 47-58.

32. D'Alessio, M., et al., Glutathione depletion up-regulates Bcl-2 in BSO-resistant cells. FASEB J, 2004. **18**(13): p. 1609-11.

33. Reddy, P.H., Inhibitors of mitochondrial fission as a therapeutic strategy for diseases with oxidative stress and mitochondrial dysfunction. Journal of Alzheimer's disease : JAD, 2014. **40**(2): p. 245-256.

34. Lin, M.T. and M.F. Beal, Mitochondrial dysfunction and oxidative stress in neurodegenerative diseases. Nature, 2006. **443**(7113): p. 787-95.

35. Jenner, P., Oxidative stress in Parkinson's disease. Ann Neurol, 2003. **53 Suppl 3**: p. S26-36; discussion S36-8.

36. Henchcliffe, C. and M.F. Beal, Mitochondrial biology and oxidative stress in Parkinson disease pathogenesis. Nat Clin Pract Neurol, 2008. **4**(11): p. 600-9.

37. Elahi, M.M., Y.X. Kong, and B.M. Matata, Oxidative stress as a mediator of cardiovascular disease. Oxidative medicine and cellular longevity, 2009. **2**(5): p. 259-269.

38. Forman, H.J., H. Zhang, and A. Rinna, Glutathione: overview of its protective roles, measurement, and biosynthesis. Mol Aspects Med, 2009. **30**(1-2): p. 1-12.

39. Ferguson, G.D. and W.J. Bridge, The glutathione system and the related thiol network in Caenorhabditis elegans. Redox Biol, 2019. **24**: p. 101171.

40. Yuan, L. and N. Kaplowitz, Glutathione in liver diseases and hepatotoxicity. Mol Aspects Med, 2009. **30**(1-2): p. 29-41.

41. Pallardo, F.V., et al., Role of nuclear glutathione as a key regulator of cell proliferation. Mol Aspects Med, 2009. **30**(1-2): p. 77-85.

42. Fiaschi, T., et al., Redox regulation of beta-actin during integrin-mediated cell adhesion. J Biol Chem, 2006. **281**(32): p. 22983-91.

43. Dikalov, S.I., et al., Nox2-induced production of mitochondrial superoxide in angiotensin II-mediated endothelial oxidative stress and hypertension. Antioxid Redox Signal, 2014. **20**(2): p. 281-94.

44. Bekeschus, S., et al., Hydrogen peroxide: A central player in physical plasma-induced oxidative stress in human blood cells. Free Radic Res, 2014. **48**(5): p. 542-9.

45. Hung, C.H.-L., et al., A reciprocal relationship between reactive oxygen species and mitochondrial dynamics in neurodegeneration. Redox biology, 2018. **14**: p. 7-19.

46. Lam, N.T., et al., Valve interstitial cell contractile strength and metabolic state are dependent on its shape. Integr Biol (Camb), 2016. **8**(10): p. 1079-1089.

47. Marquez, J.P., Fourier analysis and automated measurement of cell and fiber angular orientation distributions. International Journal of Solids and Structures, 2006. **43**(21): p. 6413-6423.

48. Valente, A.J., et al., A simple ImageJ macro tool for analyzing mitochondrial network morphology in mammalian cell culture. Acta Histochem, 2017. **119**(3): p. 315-326.

49. Leonard, A.P., et al., Quantitative analysis of mitochondrial morphology and membrane potential in living cells using high-content imaging, machine learning, and morphological binning. Biochim Biophys Acta, 2015. **1853**(2): p. 348-60.

50. Mirzapoiazova, T., et al., Monitoring and Determining Mitochondrial Network Parameters in Live Lung Cancer Cells. J Clin Med, 2019. **8**(10).

51. Xylas, J., et al., Improved Fourier-based characterization of intracellular fractal features. Opt Express, 2012. **20**(21): p. 23442-55.

52. Kolenc, O.I. and K.P. Quinn, Evaluating Cell Metabolism Through Autofluorescence Imaging of NAD(P)H and FAD. Antioxid Redox Signal, 2019. **30**(6): p. 875-889.

CHAPTER 4

CONCLUSION AND FUTURE DIRECTIONS

4.1 Conclusion

As explained in Chapter 1, assessing the dynamics of cellular structures through their organization and morphology has proven to be significantly important in understanding the behavior of certain pathological conditions [1, 2]. It was further explained that through novel imaging devices, it is possible to isolate and closely observe multiple organelles as they interact to a certain stimulus [3, 4]. However, it was also demonstrated that many of the current image analysis techniques are still behind, having problems to quantify cellular characteristics without multiple steps of processing and image segmentation [5, 6].

Throughout the experiments performed in Chapter 2 and Chapter 3, it was proven that the image analysis techniques developed were useful for fractal organization, fiber alignment, and nuclear elongation quantification. The MBM [7], being the newest among these techniques, showed sensitivity to a higher range of FD values, and proved to be efficient in both assessing mitochondrial clustering from simulated fractal clouds and NADH auto-fluorescence pictures [7]. By inducing cellular changes through the depletion of GSH with BSO in Chapter 3, it was shown that the organization and fiber orientation of actin and mitochondria changed overtime. Laser scanning confocal images showed a clear disruption of the actin cytoskeleton, which in turned affected the alignment of the mitochondria, and lastly the shape of the nuclei. Combining the image analysis of the MBM with DV and NAR, showed that these techniques can measure organization, alignment, and nuclear elongation simultaneously within the same image field on a pixel-by-pixel basis and without segmentation [7-10]. Moreover, correlations of FD, DV, NAR measurements showed a clear relation of the cellular dynamics among actin, mitochondria, and

cell nuclei, which could be used to understand the consequences and effects of damaged cellular structures in the overall state of the cell.

To summarize, with the inclusion of the new developed set of computational techniques introduced in this thesis, it is possible to measure significant cellular changes that have been observed in certain pathological conditions, and in addition, correlate these findings with other biological assessments to aid in the study of multiple mechanisms that are still not clarified.

4.2 Future directions

Techniques of image analysis are important to obtain significant measurements from digital data. As the field continues to expand, it would possible to include different cellular structures which also play important roles in maintaining cell homeostasis. Moving forward, it could also be possible to apply similar measurements at a higher scale to also quantify properties of tissue sections. As previously stated, there are still multiple cellular mechanism being explored; and as more sophisticated imaging devices and methods to contrast cellular structures continue to arise, applying these techniques will aid on clarifying the dynamics and properties behind them.

4.3 References

1. Kommaddi, R.P., et al., Abeta mediates F-actin disassembly in dendritic spines leading to cognitive deficits in Alzheimer's disease. J Neurosci, 2018. **38**(5): p. 1085-1099.

2. Yamazaki, K.G., et al., Intravenous (-)-epicatechin reduces myocardial ischemic injury by protecting mitochondrial function. Int J Cardiol, 2014. **175**(2): p. 297-306.

3. Kolenc, O.I. and K.P. Quinn, Evaluating Cell Metabolism Through Autofluorescence Imaging of NAD(P)H and FAD. Antioxid Redox Signal, 2019. **30**(6): p. 875-889.

4. Birkholz, H., et al. Quantification of Actin Filament Organization by Estimating Graph Structures in Confocal Microscopic Images. in World Congress on Medical Physics and

Biomedical Engineering, September 7 - 12, 2009, Munich, Germany. 2010. Berlin, Heidelberg: Springer Berlin Heidelberg.

5. Xylas, J., et al., Improved Fourier-based characterization of intracellular fractal features. Opt Express, 2012. **20**(21): p. 23442-55.

6. Valente, A.J., et al., A simple ImageJ macro tool for analyzing mitochondrial network morphology in mammalian cell culture. Acta Histochem, 2017. **119**(3): p. 315-326.

7. Vargas, I., et al., Rapid quantification of mitochondrial fractal dimension in individual cells. Biomed Opt Express, 2018. **9**(11): p. 5269-5279.

8. Lahn, M., C. Dosche, and C. Hille, Two-photon microscopy and fluorescence lifetime imaging reveal stimulus-induced intracellular Na+ and Cl- changes in cockroach salivary acinar cells. Am J Physiol Cell Physiol, 2011. **300**(6): p. C1323-36.

9. Quinn, K.P. and I. Georgakoudi, Rapid quantification of pixel-wise fiber orientation data in micrographs. J Biomed Opt, 2013. **18**(4): p. 046003.

10. Quinn, K.P., et al., An automated image processing method to quantify collagen fibre organization within cutaneous scar tissue. Exp Dermatol, 2015. **24**(1): p. 78-80.

APPENDIX A

MATLAB SCRIPTS

A.1 Modified Blanket Method (MBM)

This appendix contains the Matlab files used to create fractal dimension (FD) maps from images obtained using the laser scanning confocal microscope, as described in Chapter 3. The function **MBM.m** computes and maps fractal dimension on a pixel-by-pixel basis. Within this script, the user must input the value of a few variables. These variables include the value of the background intensity to isolate the region of interest (create a binary mask) as marked by the variable "**back_int**", and the size of the convolution radius as marked by the variable "**xx**". In addition, the function **MBM.m** calls **modified_blanket_2.m**, which is responsible of computing and recording the changes in local surface area as a function of image resolution. Lastly, the function **MBM.m** calls **doubleim2ind.m** which sets up the upper and bottom limits of the FD map prior to mapping.

MBM.m

```
%% Loading images
%% Place all images in the corresponding MATLAB folder
tic
clc, clear, close all

%% Select input format: "png, jpeg, tif"
files = dir('*.tif');

%% Reading images
for ii=1:length(files)
im=imread(files(ii).name);

%% Plotting original images
figure;imagesc(im);title('Original Image');colormap gray;colorbar;

%% Assigning grayscale for further analysis
for i=1:length(files),disp(files(i).name);end
```

```
im=mean(double(im),3);
imoi=mean(double(im),3);
Windows1=mat2gray(im);

%% Getting rid of background signal
%% This number is manually set depending on the quality of the image, and is
%% subject to change depending on acquisition criteria
back_int=40;
imoi=imoi-back_int;

%% Assigning intensity = 0 to the background
imoi(imoi<=0)=0;

%% Changing the range of image intensity between 0 and 1
imoi=imoi/(max(max(imoi)));
Windows2=mat2gray(imoi);

%% Plotting grayscale image
figure;imagesc(imoi);title('Background = 0');colormap gray; colorbar;

%% Modified Blanket analysis
%% Select wanted convolution radius (CR)
xx=25;
Cells=im;

%% Apply the MBM function:
[sa_cells ps]=modified_blanket_2(Cells,xx);

%% Extracting pixel size and surface area data after applying the MBM
%% function:
x=log(ps);
y=log(sa_cells);

%% Getting rid of first value to improve accuracy:
x=x(2:xx);
y=y(:,:,2:xx);

%% Computing slope:
slope(:,:,1)=(y(:,:,2)-y(:,:,1))/(x(2)-x(1));
for i=2:(length(x)-1)
    slope(:,:,i)=(y(:,:,i+1)-y(:,:,i-1))/(x(i+1)-x(i-1));
end
slope(:,:,length(x))=(y(:,:,length(x))-y(:,:,length(x)-1))/(x(length(x))-
x(length(x)-1));
for i=1:xx;
    x(i)=(mean(mean(sa_cells(:,:,i),1),2));
end

%% Creating FD Map
FDmap=real(2-mean(slope(:,:,1:end),3));
FDc=doubleim2ind(FDmap,2.7,2.5);
FDc=ind2rgb(FDc,jet(256));
FDmap(isnan(FDmap))=0;
FDmap(isinf(FDmap))=0;

%% Isolating FD Signal based on image intensity
```

```
%% This creates a binary mask with the ROI
Signal=double(imoi>0.075);
se = strel('disk',5);

%% Image operations to improve mask:
%% "erosion, dilation, closing, and opening"
%% Recall some of these may be skipped if not needed
Signal = imdilate(Signal,se);
Signal = imclose(Signal,se);
Signal = imopen(Signal,se);
Signal = imerode(Signal,se);

%% Isolating pixels within the ROI of the FD Map
Av_FD=FDmap.*(Signal);

%% Plotting binary mask and FD Map for assessment of ROI
figure;imagesc(Signal);colormap gray
figure;imagesc(FDc.*imoi.*Signal);title('Average Local FD (Intensity
image)');colormap jet;colorbar;caxis([2 4]);

%% Calculating average FDwithin the ROI
Average_FD1=(sum(sum(Av_FD))/(sum(sum(Signal))));
Fractal_dim1(ii)=(sum(sum(Av_FD))/(sum(sum(Signal))));
clear('slope')

%% Saving FD Maps and resultant images after processing:
imwrite(FDc.*imoi.*Signal,sprintf('%s FD %d.png',files(ii).name,xx))
imwrite(Signal,sprintf('%s Mask.png',files(ii).name))
imwrite(Windows1,sprintf('%s.png',files(ii).name))
imwrite(Windows2,sprintf('%s No back.tif',files(ii).name))
close all
end

%% Obtaining table of average FD values:
FD_values1=Fractal_dim1';
toc
```

modified_blanket_2.m

```
%% MBM function (separate m-file) with descriptions:
function [side_surface_cloud pixel_size_cloud]= modified_blanket(cloud,sz);
% This function approximates the fractal dimension of cell images.
% cloud = original image to be analyzed
% sz = size of the convolution disk

%% Modified Blanket Method - Main image, kernels, and convolution disk
Image=cloud;
kernel_hor=[1 -1 0];
kernel_ver=[0;-1;1];
hk=fspecial('disk',sz)*sz^2*pi;
j=0;

%% Resizing and Convolution Loop
for i=sz:-1:1
    size(Image,1):-2:round(size(Image,1)/(2/sqrt(2)*sz));
```

```
    newimsize=round(i/sz*size(Image,1));
    hk2=imresize(hk,[i i]);

    j=j+1;
    Image_resized=imresize(Image,[newimsize newimsize]);

    Imagef_hor=imfilter(Image_resized,kernel_hor,'symmetric');
    Imagef_ver=imfilter(Image_resized,kernel_ver,'symmetric');
    Ih=imfilter(abs(Imagef_hor),hk2,'symmetric');
    Iv=imfilter(abs(Imagef_ver),hk2,'symmetric');

side_surface_cloud(:,:,j)=imresize(size(Image,1)/i/sz*(Ih+Iv),size(Image));
pixel_size_cloud(j)=size(Image,1)/i*sz;
end
end
```

doubleim2ind.m

```
function [B]=doubleim2ind(A,uplim,botlim)

B=(A-botlim)*(255/(uplim-botlim));
  B=double(uint8(B));

end
```

A.2 Nuclear Aspect Ratio (NAR)

This appendix contains the Matlab files used to compute and map changes in nuclear aspect ratio (NAR) from images obtained using the laser scanning confocal microscope, as described in Chapter 3. The function **NAR.m** computes and maps changes in the nucleus by measuring the axis properties of each nuclei after being isolated with a binary mask. Within this script, the user must input the value of a few variables. These variables include the value of the background intensity to isolate the region of interest (create a binary mask) as marked by the variable "**back_int**", and the size of the erosion radius to remove non-nuclear articfacts as marked by the variable "**se**". The **NAR.m** also calls **doubleim2ind.m** to set up the upper and bottom limits of the NAR map prior to mapping.

NAR.m

```
%% Place all images in the corresponding MATLAB folder
tic
clc, clear, close all

%% Select input format: "png, jpeg, tif"
files = dir('*.png');

%% Loading images
for ii=1:length(files)
im=imread(files(ii).name);

%% Plotting original images
figure;imagesc(im);title('Original Image');colormap gray;colorbar;

%% Assigning grayscale for further analysis
for i=1:length(files),disp(files(i).name);end
imoi=mean(double(im),3);
raw=mat2gray(imoi);

%% Saving grayscale images
imwrite(raw,sprintf('%s.png',files(ii).name))

%% Getting rid of background signal
%% This number is manually set depending on the quality of the image, and is
%% subject to change depending on acquisition criteria
back_int=20;
imoi=imoi-back_int;

%% Assigning intensity = 0 to the background
imoi(imoi<=0)=0;

%% Assigning intensity = 0 to the background
imoi=imoi/(max(max(imoi)));

%% Isolating FD Signal based on image intensity
%% This creates a binary mask with the ROI
Signal=double(imoi>0);

%% Image operations to improve mask:
%% "erosion, dilation, closing, and opening"
%% Recall some of these may be skipped if not needed
se = strel('disk',5);
Signal = imdilate(Signal,se);
Signal = imclose(Signal,se);
se = strel('disk',5);
Signal = imerode(Signal,se);

%% Plotting binary mask
figure;imagesc(Signal);title('Mask');colormap gray; colorbar;

%% NAR Calculations
%% bwlabel is used to count the amount of cells
[SG, L(ii)] = bwlabel(Signal);
```

```
%% Applying region props to extract characteristics of the binary mask:
props=regionprops('table',SG,'Area','MajorAxisLength','MinorAxisLength','Peri
meter')
Area=props.Area;
Major=props.MajorAxisLength;
Minor=props.MinorAxisLength;
Perimeter=props.Perimeter;
Circularity = (4 * pi * Area)./ (Perimeter .^ 2);
SG1=SG;

%% Getting rid of non-nuclei artifacts
%% This is done based on the total area in pixels of the nuclei artifacts
for nn=1:L(ii)

if Area(nn)<350
    Major(nn)=0;
    Minor(nn)=0;
    Ratio(nn)=0;
    L(ii)=L(ii)-1;

else
    Ratio(nn)=Major(nn)/Minor(nn);
end
end

%% Computing average NAR
Av_ratio(ii)=sum(Ratio)/L(ii);
Ratio_map=Ratio;
clear Ratio

for kk=1:max(max(SG1))
SG1(SG1==kk)=Ratio_map(kk);
end
Signal_1=SG1>0;

%% Saving binary mask
imwrite(Signal_1,sprintf('%s Mask.png',files(ii).name))


%% Creating Aspect Ratio Map
FDc=doubleim2ind(SG1,2,1);
FDc=ind2rgb(FDc,jet(256));
FDmap(isnan(FDc))=0;
FDmap(isinf(FDc))=0;

%% Plotting and saving NAR Map
figure,imagesc(FDc.*imoi),colormap jet,caxis([1 2]);
imwrite(FDc.*imoi,sprintf('%s NucMap.png',files(ii).name))
close all
end

%% Creating data table with Average NAR and number of cells per image field
Nuc_data=[Av_ratio' L']
toc
```

APPENDIX B

IBC LETTER

UNIVERSITY OF ARKANSAS

Office of Research Compliance

August 14, 2019

MEMORANDUM

TO:	Dr. Kyle Quinn
FROM:	Ines Pinto, Biosafety Committee Chair
RE:	Protocol Renewal
PROTOCOL #:	17010
PROTOCOL TITLE:	Optical characterization of cell metabolism
APPROVED PROJECT PERIOD:	**Start Date** September 8, 2016 **Expiration Date** September 7, 2022

The Institutional Biosafety Committee (IBC) has approved your request, dated July 21, 2019, to renew IBC # 17010, "Optical characterization of cell metabolism".

The IBC appreciates your assistance and cooperation in complying with University and Federal guidelines for research involving hazardous biological materials.

1424 W. Martin Luther King, Jr. • Fayetteville, AR 72701
Voice (479) 575-4572 • Fax (479) 575-6527